

1 **Combining topology and fractal dimension of fracture networks to**
2 **characterise structural domains in thrust limestones**

3 Mark W. Grodner *^a, Stuart M. Clarke^a, Stuart D. Burley^{a, b}, A. Graham
4 Leslie^{a, c}, Richard Haslam^{a, d}

5 ^a Basin Dynamics Research Group, School of Geography, Geology and the
6 Environment, Keele University, Keele, ST5 5BG, United Kingdom,

7 m.w.grodner@keele.ac.uk, +44 (0) 1782 734301

8 s.m.clarke@keele.ac.uk

9

10 ^b Discovery Geoscience, Lapworth Croft Lodge, Lapworth, United Kingdom,

11 stuart.burley@discovery-geoscience.com

12

13 ^c British Geological Survey, Lyell Centre, Research Avenue South,

14 Edinburgh EH14 4AP, United Kingdom, agle@bgs.ac.uk

15

16 ^d British Geological Survey, Keyworth Centre, Nicker Hill, Keyworth,

17 Nottingham NG12 5GG, United Kingdom, richas@bgs.ac.uk

18

19 Keywords: fractal dimension, topology, fracture pattern, fold-thrust

20

21 **Highlights**

- 22 • A new method for characterising fractures in fold-and-thrust belts
23 with complex fracture networks
- 24 • Reduced time for data collection compared to traditional techniques
- 25 • Fractal dimensions and topology are combined to characterise
26 fractures in structural domains
- 27 • Fore-thrusts and back-thrusts have higher fractal dimensions than
28 pop-up structures
- 29 • Fore-thrusts have fewer longer fractures, back-thrusts have higher
30 densities of connected fractures

31 **Abstract**

32 Fractures in limestones of the Palaeocene Lockhart Formation in the
33 hanging wall of the Himalayan Main Boundary Thrust north of Islamabad
34 are examined, and the data analysed using a combination of topology and
35 fractal dimension to characterise fracture patterns and relate them to
36 structural domains. Neither technique alone allows the recognition of the
37 structural domains. However, when considered together for all the fractures
38 within an area, fore-thrusts, pop-ups and back-thrusts can be
39 distinguished. The fractures are considered together, as the characteristics
40 of the individual structural domains are characterised by the cumulative
41 effect of all the different fractures, and in these complexly fractured rocks,
42 the concept of fracture sets is problematic. Fore- and back-thrusts have
43 higher fractal dimensions than pop-up structures. The highest fractal
44 dimensions of both types of thrusts occur immediately adjacent to and
45 decrease away from the central pop-up structure. Topologically, fore-thrust
46 domains have fewer fractures and fracture intersections (nodes), with a
47 longer mean fracture trace length; back-thrust domains contain more
48 nodes (hence also more tips, lines, and branches) resulting in higher
49 fracture densities. Pop-up structure domains are characterised by a low
50 fracture intensity. Using the combined analysis of both the topology and
51 fractal dimension, we show that the fracture pattern characteristics are
52 predictable when related to the different structural settings identified within
53 fold and thrust of the Lockhart Formation.

54

55 **1. Introduction**

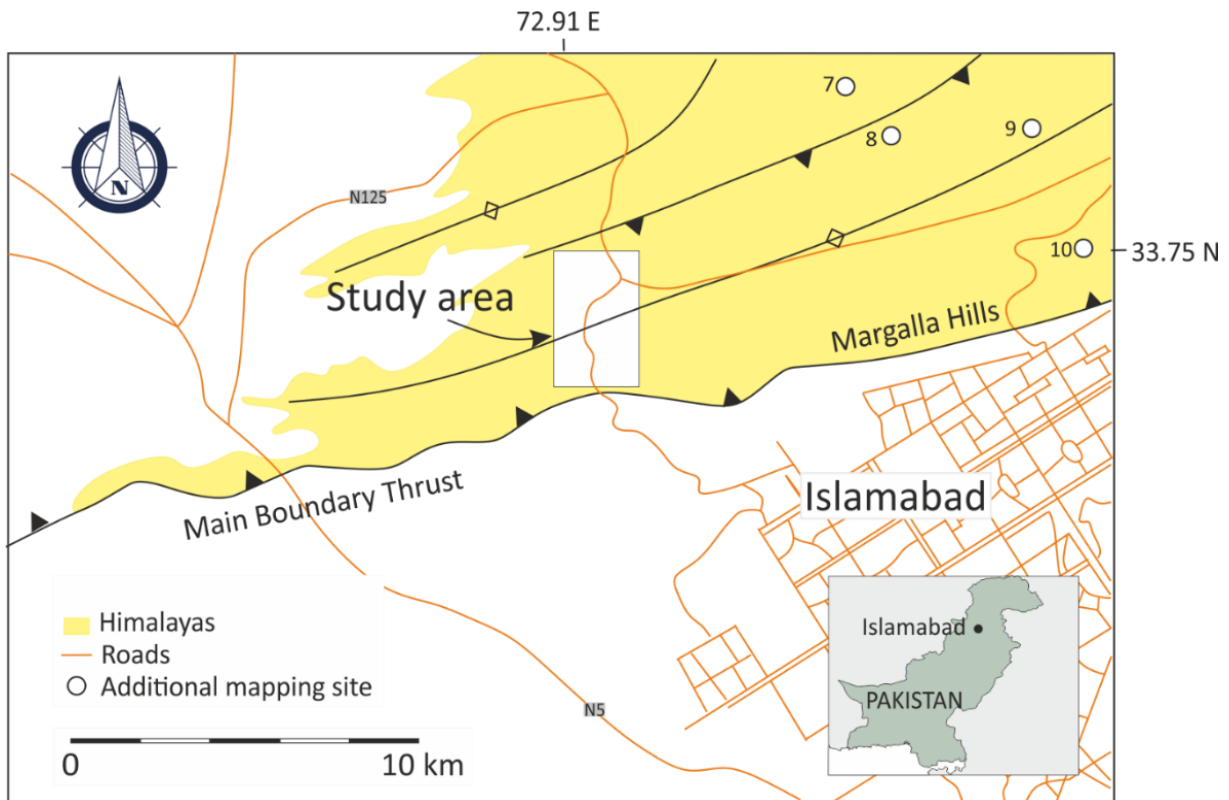
56 Fracturing of a rock mass is a mechanical response to an applied stress
57 (e.g., Ramsay, 1967; Long *et al.*, 1996), with the extent and characteristics
58 of the resultant fracture network controlled by the mechanical properties of
59 the rock mass, fluid characteristics, and variations in the stress field
60 (e.g., Laubach *et al.* 2019). Understanding the properties and

61 characteristics of the resultant fracture network is essential in many
62 aspects of applied geoscience, from determining the stability of an
63 excavation (Hoek and Brown, 1980) to identifying fluid pathways and
64 storage volumes for minerals (Cox, 2005) or hydrocarbons (Aydin, 2000).

65 Fracture systems are defined as geometrical arrays of linked and often
66 interacting fractures within a rock mass (Rouleau and Gale, 1986; Odling
67 *et al.*, 1999). Fracture systems have attracted much scientific attention and
68 numerous methods have been proposed to characterise them, ranging from
69 analysis of their kinematic behaviour, through shared and/or discrete
70 geometry, to tectonic setting, as concisely and instructively summarised by
71 Peacock and Sanderson (2018).

72 The geometric arrangements of fractures in a rock volume are typically
73 viewed as either discrete objects in space (Barros-Galvis, *et al.*, 2015;
74 Welch *et al.*, 2015), or topologically, that is to say, 'in relation to one
75 another' (Long and Witherspoon, 1985; Laubach *et al.*, 2018), and/or in
76 direct relation to causative mechanisms.

77



78

79 Figure 1: Location of the principal study area and additional mapping sites
 80 (7 to 10) in the foothills of the Himalayas north of Islamabad, Pakistan.
 81 Several tectonic structures are developed in the hanging wall strata of the
 82 Main Boundary Thrust and they form the focus of this study.

83 Studies that consider the spatial distribution of fractures as discrete objects
 84 provide valuable insights into the relationships between fractures and
 85 lithological characteristics of the fractured rock mass. For example, the
 86 spacing of fractures commonly varies with lithology or, more correctly, with
 87 differences in the mechanical properties of the lithology, such that
 88 competent lithologies display more widely-spaced fractures, for a given
 89 stress, compared to their less competent counterparts (Pollard and
 90 Fletcher, 2005; Ortega *et al.*, 2010; Hooker *et al.*, 2013). Fracture spacing
 91 also varies with bed thickness (Ladeira and Price, 1981) with thicker beds
 92 containing more widely-spaced fractures than their thinner equivalents, for
 93 a given stress. In folded strata, differences in the geometry of fracture
 94 patterns are related to variations in competence and bed thickness and a
 95 response to the complex strain distribution in fold systems. This results in

96 a broad array of geometrical fracture characteristics associated with
97 ductile/brittle-ductile fold deformation features (Cosgrove, 2015; Ferrill *et*
98 *al.*, 2016).

99 By contrast, topological analysis of a fracture network characterises the
100 connectivity of the constitutive fractures in that network, rather than the
101 inherent properties of the individual fractures (Sanderson *et al.*, 2019). This
102 approach has provided an improved understanding of the overall behaviour
103 of the physical properties of the rock mass under consideration, particularly
104 in terms of its strength, porosity, and permeability (Sanderson and Nixon,
105 2015).

106 Approaches to fracture characterisation that establish a causative
107 relationship between a particular fracture system and the mechanism
108 responsible for its formation require observations that can indicate a
109 temporal link between a fracture network and the proposed process (Long,
110 *et al.*, 1996). Examples include studies of how fracture systems of different
111 ages (established by geochemistry) link together to control mineralisation
112 within Archean orogenic gold (Dziggel *et al.*, 2007) or recognition of
113 mining-induced fractures and pre-existing geological discontinuities and
114 how they interact to produce the rock mass around a mining stope
115 (Grodner, 1999).

116 The task of relating a fracture system to a specific process is particularly
117 challenging for rocks that have been subjected to multiple deformational
118 events. For example, in fold-and-thrust belts deformation results from a
119 combination of burial, changes in fluid pressure and composition, folding,
120 thrusting, uplift and exhumation (Engelder *et al.*, 1985; English and
121 Laubach, 2017). The distribution of fractures variously reflects the different
122 failure responses to stresses of these events due to variations in mechanical
123 properties of the rock mass (Wennberg *et al.*, 2006), that themselves
124 evolve through time (Laubach *et al.*, 2009). Progressive folding can also
125 result in multiple generations of opening-mode fractures (Cosgrove, 2015).
126 Consequently, polyphase deformation in fold-and-thrust belts typically

127 results in complex, sequential overlays of fracture networks with such high
128 abundances and intricate patterns that they are not readily described by
129 simple fold-fault-fracture geometries (Cosgrove, 2015), or by one-
130 dimensional descriptors (Watkins *et al.*, 2015; Laubach *et al.*, 2018).
131 Fractures formed at the same time can have different orientations and
132 mineral compositions and conversely fractures formed at different times
133 can have the same orientations or mineralisation (Laubach *et al.*, 2019).
134 To properly quantify the effects of the fracture networks on the rock mass,
135 the whole fracture system must be considered rather than apparently
136 discrete fracture sets in a fracture network (Peacock *et al.*, 2018).

137 Here we present a novel approach to the challenges involved in developing
138 an informative, and potentially predictive, characterisation of highly
139 fractured rock. The individual constituent fracture types within the fracture
140 system are not separated for analysis, but rather we consider how the
141 cumulative effects can be used to discriminate different structural domains.
142 This approach integrates discrete topological and spatial methods for
143 characterising fractures and fracture networks by employing fractal
144 dimension to provide a spatial context of the distribution of the constituent
145 fractures, and then combining those data with analyses of the observed
146 topological relationships and interconnectivity of the fracture networks. The
147 approach provides a more robust assessment and analysis of the fractures
148 observed within the rock mass and their characteristics than can be
149 achieved from application of either method in isolation. As we consider all
150 the topological and fractal data together, all the interactions between
151 fractures, and their effects upon the characteristics of the rock mass are
152 defined. Moreover, this approach dramatically reduces the time taken for
153 data collection compared to traditional fracture sampling techniques and
154 provides large amounts of unbiased data representative of fracture network
155 characteristics over a wide range of fracture structural domains.

156 We apply this technique to examine the occurrence and distribution of
157 fracturing in well-exposed in Palaeocene limestones within the frontal thrust

158 sheets associated with the Main Boundary Thrust (MBT) of the Himalayan
159 fold and thrust belt (Tariq *et al.*, 2017; Dasti *et al.*, 2018), in a region
160 approximately 10 km north of Islamabad, NW Pakistan (Figure 1 and Figure
161 2). Here, in a single stratigraphic unit (the Lockhart Limestone) a complex
162 sequence of fractures can be studied across fore-thrusts, back-thrusts, and
163 pop-up structures that all occur above, and immediately to the north of the
164 MBT. We recognise that there are multiple generations of fractures in the
165 study area, but as the geomechanical properties of the rock mass must be
166 the result of all fractures combined, we contend that it is important to
167 consider all fractures collectively to understand differences in the
168 cumulative distribution of fracture sets related to specific structures.
169 Restricting the structural analysis to a single stratigraphic unit removes
170 variation in fracture characteristics related to lithology.

171 **2. Regional Geological Setting**

172 The geology of the study area, in the Potwar Basin of northern Pakistan,
173 immediately adjacent to the capital city of Islamabad (**Error! Reference**
174 **source not found.**), is dominated by sedimentary deposits and structural
175 features associated with the collision of the Indian and Eurasian plates
176 during the Himalayan Orogeny (Acharyya and Saha, 2018). Continual
177 southwards-directed and décollement-related thrusting of the crust of the
178 Indian Plate resulted in a variety of high-level fold and fault structures in
179 the hanging walls of the major thrusts that crop out in northern Pakistan
180 (Yeats and Hussain, 1987; Pivnik and Wells, 1996; Burg *et al.*, 2005). As
181 one of these major thrusts, the MBT is a regional-scale structure that
182 demarcates the southern limit of the Peshawar-Hazara Basin, transporting
183 a Mesozoic-Tertiary marine sequence of the Indo-Pakistan Plate south-
184 eastwards over the syn-tectonic molasse of the Murree Formation
185 sediments (Iqbal and Bannert, 1998; Ghani *et al.*, 2018).

186 Sediments ranging from Precambrian evaporite, through Permian and
187 Triassic siltstone-dominated sequences to successions of Jurassic
188 sandstone, shale and limestone are present locally, but do not crop out in

189 the study area and hence are not considered further. All analyses were
190 undertaken on limestone units of the Palaeocene Lockhart Formation
191 (Figure 2) which were deposited unconformably over Cretaceous fluvial and
192 marine sediments on the northern leading edge of the Indian Plate during
193 the closure of the Palaeo-Tethys Ocean (Chatterjee and Bajpal, 2016).
194 Strata of the Lockhart Formation comprise a series of stacked
195 foraminiferal–algal build-ups intercalated with argillaceous siltstone and
196 mudstone, all deposited in cyclical units on a low-energy shelfal carbonate
197 ramp, with the sediments recording many shallowing and shoaling events
198 from open marine to inner ramp conditions (Hanif *et al.*, 2014). The
199 limestone units of the formation generally comprise lime-mudstone,
200 argillaceous wackestone and, more rarely, packstone, all with little or no
201 primary matrix porosity.

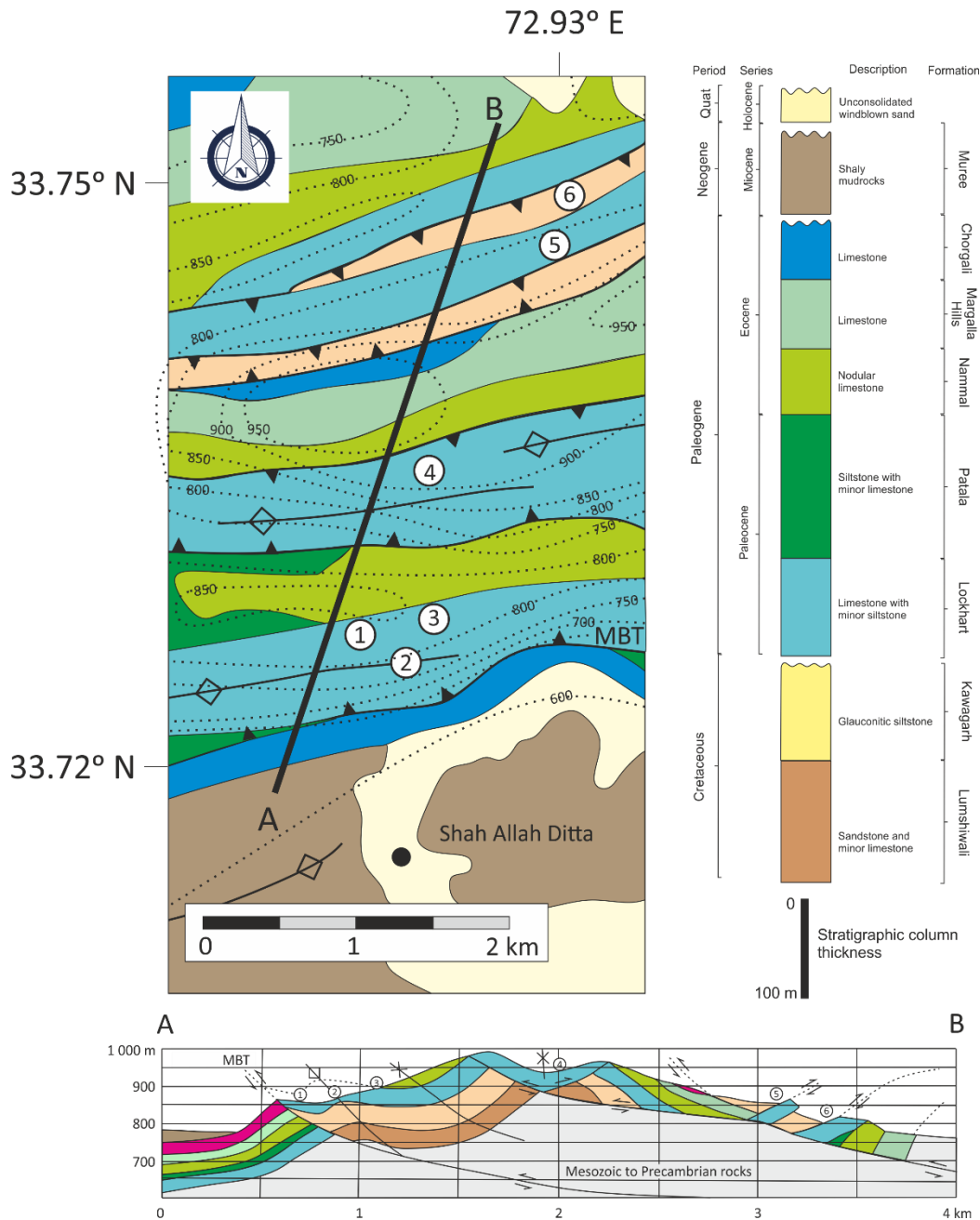
202

203 Strata of the Lockhart Formation are overlain by siltstone and limestone of
204 the late Palaeocene Patala Formation and the Eocene Nammal and Margalla
205 Hill formations. This is a result of continued conformable deposition on a
206 low-energy, shallow-marine shelf that shallows to a lagoonal and supratidal
207 setting by the end of the Eocene Epoch (Hanif *et al.*, 2014; Wandrey *et al.*,
208 2004).

209

210 Eocene strata are overlain unconformably across the whole of the Potwar
211 Basin by Miocene fluvial sediments (Wandrey *et al.*, 2004) that record
212 deposition of post-initial collision Himalayan molasse. Pleistocene and
213 Holocene superficial deposits complete the depositional record and consist
214 of windblown silt and sand, along with alluvial gravel adjacent to the active
215 thrust scarps (Robert *et al.*, 1997).

216



217

218 Figure 2: Geology of the study area with the positions of the primary study
 219 sites in the transect line indicated by numbers. Surface elevations in metres
 220 above mean sea level are indicated by dotted lines on the map. Dotted lines
 221 on the cross-section are projections of the strata. MBT = Main Boundary
 222 Thrust. This dataset is augmented by further data from four sites 15 km
 223 northeast along strike (Figure 1). Geological map modified after Ali (2014)
 224 to conform with field mapping undertaken in this study. Interpretations of
 225 deeper levels on the cross section are from Williams *et al.* (1997). Vertical
 226 exaggeration: x4.

227 **3. Methodology**

228 3.1 Nomenclature and site selection

229 The dataset used to test the method described in this study comprises field
230 measurements of fractures in the limestone-dominated strata of the
231 Lockhart Formation associated with the MBT in northern Pakistan. These
232 strata display a spectrum of brittle geomechanical behaviours across a
233 range of scales, within units of limestone with very low porosity,
234 interbedded with units of argillaceous siltstone and mudstone. By
235 restricting collection of fracture data to locations within the well-exposed
236 Palaeocene Lockhart Formation only, we remove the effects of lithological
237 variation upon the dataset. Furthermore, all of the fractures characterised
238 are located within the hanging wall of the MBT (Robert *et al.*, 1997; Iqbal
239 and Bannert, 1998), and all have been subjected to the same regional
240 tectonic stress field. For clarity, fracture nomenclature and terminology
241 adopted in this study are summarised in Table 1.

242

243 Table 1: Nomenclature and descriptive terminology as applied in this study.

| Term | Meaning |
|----------------------------------|--|
| Fracture | Sub-planar, brittle discontinuity separating the mechanical properties of a rock. It is very narrow in width relative to the other two dimensions. The term considers extension fractures (joints and veins) as well as shear fractures with negligible displacement sub-parallel to the fracture (Peacock <i>et al.</i> , 2018). |
| Fracture set and fracture system | A fracture set is a subsection of a fracture system within a rock mass with similar properties (Peacock <i>et al.</i> , 2018). Properties could include orientation, mineralisation, or genetic origin. The cumulative characteristics of a fracture system are formed by the interaction of different fracture sets that need to be |

| | |
|----------------------------|--|
| | considered together to define the rock mass characteristic |
| Rock mass | A matrix consisting of intact rock and associated fractures. The properties of a rock mass are a product of the intact rock and of the fractures (Bieniawski, 1973; Barton, <i>et al.</i> , 1974; Laubscher, 1977). |
| Nodes | Terminations and intersections of fractures used in the topological analysis of the fracture data (Sanderson and Nixon, 2015). |
| Measurement circle and box | A one metre diameter circle drawn on a scaled digital photograph of rock exposure and used to define the measurement area for topological analysis. A one metre wide square box is centred on the circle and used to generate the box-counting grids for determination of the fractal dimension. |
| Fractal dimension | A quantification of the self-similarity or scale invariance of a fracture network. There are numerous methods to quantify the fractal dimension but in this study, we employ the box-counting method (see Figure 6 and Figure 7). |
| Topology | Quantification of the arrangement of fractures and how they are connected, from which it is possible to derive the physical characteristics of fractures, including fracture density, fracture intensity, mean fracture trace length, and the number of fracture tips, lines, and branches. |

244

245

246 Six principal sites were chosen to examine the differences in fracture
247 characteristics related to successive major structures (fore-thrust, pop-up,
248 and back-thrust) of the Himalayan fold and thrust belt (Figure 2). To
249 increase the geographical extent of the dataset, further data were acquired
250 from four sites located along strike (and approximately 15 km northeast)
251 of the major structural features observed in the primary transect line (Table
252 2), thereby expanding the significance of the analysed results and their
253 interpretation. All sites lie within the Margalla Hills, approximately 10 km
254 north of Islamabad, Pakistan (Figure 1). The brittle limestone and
255 interbedded subordinate mudstone of the Lockhart Formation observed at
256 all these sites are highly deformed and fractured. The study area is, as a
257 whole, contained within a series of south-verging thrusts, north-verging
258 back-thrusts, and associated folds and pop-up structures, all located within
259 the hanging wall of the MBT (Tariq *et al.*, 2017; Dasti *et al.*, 2018).

260

261 Table 2: Locations and structural styles of the sites examined in the
 262 Lockhart Formation. Sites 7 to 10 are additional supporting sites located
 263 along strike from the main transect line formed from sites 1 to 6 (see Figure
 264 1 and Figure 2).

| Site | Latitude (° N) | Longitude (° E) | Structure |
|------|----------------|-----------------|-------------------------------------|
| 1 | 33.724 | 72.917 | Fore-thrust with trailing anticline |
| 2 | 33.723 | 72.921 | Fore-thrust with trailing anticline |
| 3 | 33.726 | 72.926 | Fore-thrust with trailing syncline |
| 4 | 33.733 | 72.922 | Pop-up anticline |
| 5 | 33.745 | 72.934 | Back-thrust |
| 6 | 33.750 | 72.933 | Back-thrust |
| 7 | 33.799 | 73.074 | Back-thrust |
| 8 | 33.781 | 73.063 | Back-thrust |
| 9 | 33.778 | 73.079 | Pop-up anticline |
| 10 | 33.779 | 73.060 | Fore-thrust |

265

266 Outcrop-scale geological data captured from each site (Table 2 and
 267 Figure 2) include the lithologies present, bedding thickness, and the types
 268 of sedimentary features preserved. All exert a significant role in defining
 269 rock mass behaviour and will thus influence the structures developed during
 270 deformation (Ortega *et al.*, 2010; Hooker *et al.*, 2013; Procter and
 271 Sanderson, 2018).

272 Individual fractures have lateral extents on the scale of centimetres to
 273 millimetres and vary in type and orientation within a small area (Figure 3);
 274 characterising each individual fracture is therefore impractical at the
 275 outcrop scale in these strata. Moreover, the wide range of fracture strikes

276 at any one measurement site means that the one-dimensional scanline
277 technique (Guerriero *et al.*, 2010) will have a strong bias as fractures that
278 are sub-parallel to the scanline are less likely to be intersected by it. For
279 such inherently two-dimensional patterns, techniques of rectangular or
280 circular window mapping (Mauldon *et al.*, 2001; Watkins *et al.*, 2015) are
281 preferable. A significant advantage of these techniques is the opportunity
282 to derive topological information from these observations (Mauldon *et al.*,
283 2001; Sanderson and Nixon, 2015).

284 In these complexly fractured rocks, the concept of fracture sets is
285 problematic. Sets are typically defined as fractures sharing a narrow range
286 of orientations and (broadly) contemporaneous based on relative timing
287 information captured by fracture patterns (abutting and crossing relations)
288 or distinctive mineral deposits (Hancock, 1985). In our investigations,
289 where progressive deformation resulted in formation of numerous fractures
290 in the same deformation event, orientation and other typical aspects of sets
291 are unreliable markers of relative timing and set membership. The timing
292 complexities in our work, which could arise from fracture cement fill
293 sequences (Laubach *et al.* 2019) interactions with fracture tip propagation
294 dynamics (Renshaw and Pollard, 1994), and other processes (Long *et al.*,
295 1996), are impractical to work out without in-depth petrographic analysis,
296 which would inhibit effective characterisation of the fracture network at a
297 wider scale. To effectively define the ensemble fracture characteristics, we
298 measure use an approach to document all the fractures together.

299 At each sampling location a circle of 1 m in diameter was marked onto the
300 outcrop and captured through a minimum of four high-resolution digital
301 photographs taken to cover a 1 m by 1 m square centred upon the
302 measurement circle. Several circular windows were mapped at each
303 sampling site, on surfaces oriented both parallel to and perpendicular to
304 bedding, and on surfaces created by road-excavations at oblique angles to
305 bedding (Table 3). Analyses of the fracture characteristics at each of the

306 sampling sites are based on the combined data of all the circular windows,
307 thereby reducing orientation bias.

308 Table 3: Number of circular windows and their orientations relative to
309 bedding at the measurement sites along the transect.

| Site | Mapping points | | | |
|-------|----------------|---------------|---------|-------|
| | Parallel | Perpendicular | Oblique | Total |
| 1 | 3 | 2 | 1 | 6 |
| 2 | 1 | 1 | 2 | 4 |
| 3 | - | 2 | - | 2 |
| 4 | 1 | 1 | - | 2 |
| 5 | 1 | - | 2 | 3 |
| 6 | 1 | 1 | 1 | 3 |
| Total | 7 | 7 | 6 | 20 |

310

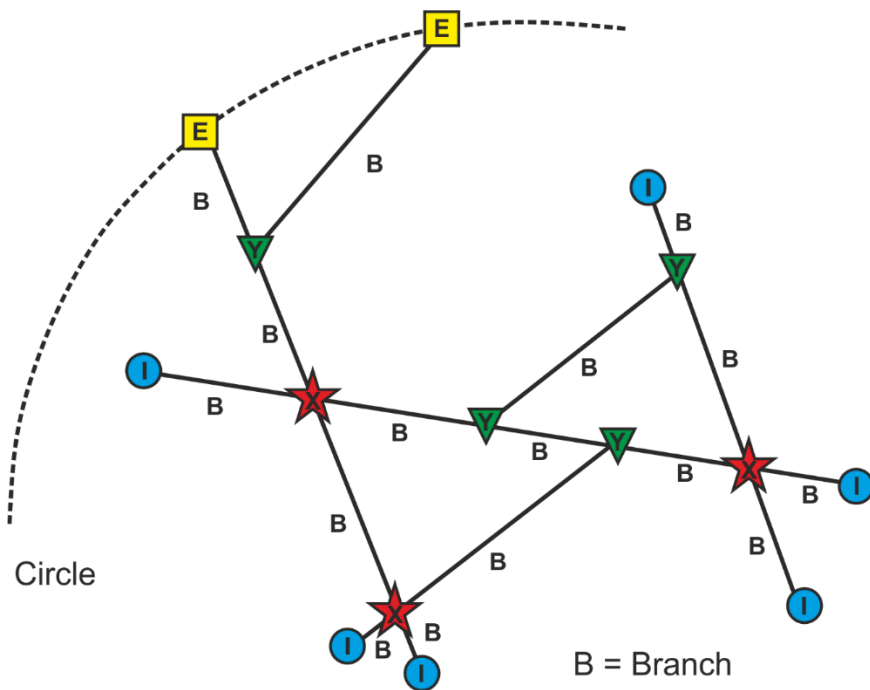
311 *3.1 Determination of topological characteristics*

312 Topology describes the way in which constituent parts of a system are
313 arranged, interrelated, and connected. The arrangement of components
314 within a geometrical system – in this case, a fracture network – can be
315 defined in terms of topology, and an analysis of that arrangement can
316 provide critical information on network pathways. For example, a high
317 number of cross-cutting fractures suggests interlinked networks with
318 continuous pathways between them. The topological characteristics of a
319 fracture network can be determined at any scale (Sanderson and Nixon,
320 2015).

321 The types of intersections (termed 'nodes') between fracture traces present
322 within the measurement circles at each of the sites in this study were
323 characterised. The types of nodes are defined as follows (Mauldon *et al.*,
324 2001; Sanderson and Nixon, 2015), and are identified in all subsequent
325 diagrams by the colour and shape indicated in parenthesis (Figure 3):

- 326 • X nodes (red star) – intersections of fracture traces that cross each
327 other and continue,
- 328 • Y nodes (green triangles) – termination of one fracture trace against
329 another fracture trace,
- 330 • I nodes (blue circles) – termination of a fracture trace within the rock
331 mass contained within in the circle,
- 332 • E nodes (yellow squares) - intersections of fracture traces with the
333 edge of the circle where the traces continue out with the circle.

334 The nodes separate fracture traces into segments known as branches. X
335 nodes have four branches, Y nodes have three, and I and E nodes have one
336 branch each (Figure 3).



337

338 Figure 3: Node types of intersecting fracture traces as defined by
339 Sanderson and Nixon (2015). Fracture branches are labelled "B". Every X
340 (red star) node has four branches, every Y (green triangle) node has three

341 branches and every I (blue circle) or E (yellow square) node has one
342 branch.

343 By counting the quantity and types of the nodes in the various
344 measurement circles we were able to determine the topological
345 characteristics of the fracture network from the following the methodology
346 of Sanderson and Nixon, (2015). The number of fracture trace terminations
347 within the circle is the sum of the number of I-nodes (N_I) and the number
348 of Y-nodes (N_Y). The number of fracture traces contained within the circle
349 (N_L) is half of the number of terminations as each trace is terminated at
350 each end by either an I- or Y-node. Consequently:

$$351 \quad N_L = \frac{1}{2}(N_I + N_Y)$$

352 As each fracture branch (Figure 3) has two nodes, with an I-node forming
353 one termination of a branch, a Y-node terminating three branches and an
354 X-node terminating four branches, the number of branches (N_B) may be
355 calculated from:

$$356 \quad N_B = \frac{1}{2}(N_I + 3N_Y + 4N_X)$$

357 The number of connections per line is a measure of fracture connectivity
358 (F_c) that describes the degree of interlinking of the fractures. It is defined
359 by:
360

$$361 \quad F_c = \frac{4(N_X + N_Y)}{N_Y + N_I}$$

362 The parameters of fracture intensity, density and mean trace length are
363 derived from the nodes with the following relationships (Mauldon *et al.*,
364 2001):
365

- 366 • Fracture Intensity, (F_I) is a comparative measure of the number of
367 edge-nodes (N_E), within a measurement circle (of radius r) and is
368 defined by:

$$369 \quad F_I = \frac{N_E}{4r}$$

370 • Fracture Density (F_D) represents the number of fractures per unit
 371 area. As a fracture is terminated inside a measurement circle of
 372 radius r by either a Y or an I node, the density is given by:

$$F_D = (N_Y + N_I) / 2\pi r^2$$

373
 374 • The Mean Trace Length (MTL) provides an estimate of the average
 375 fracture trace length as it considers the number of fractures that are
 376 contained within the measurement circle of radius r and the number
 377 that transect it. It is derived from multiplying Intensity by area and
 378 dividing by number of lines:

$$MTL = \frac{\frac{N_E}{N_Y + N_I} \pi r}{2}$$

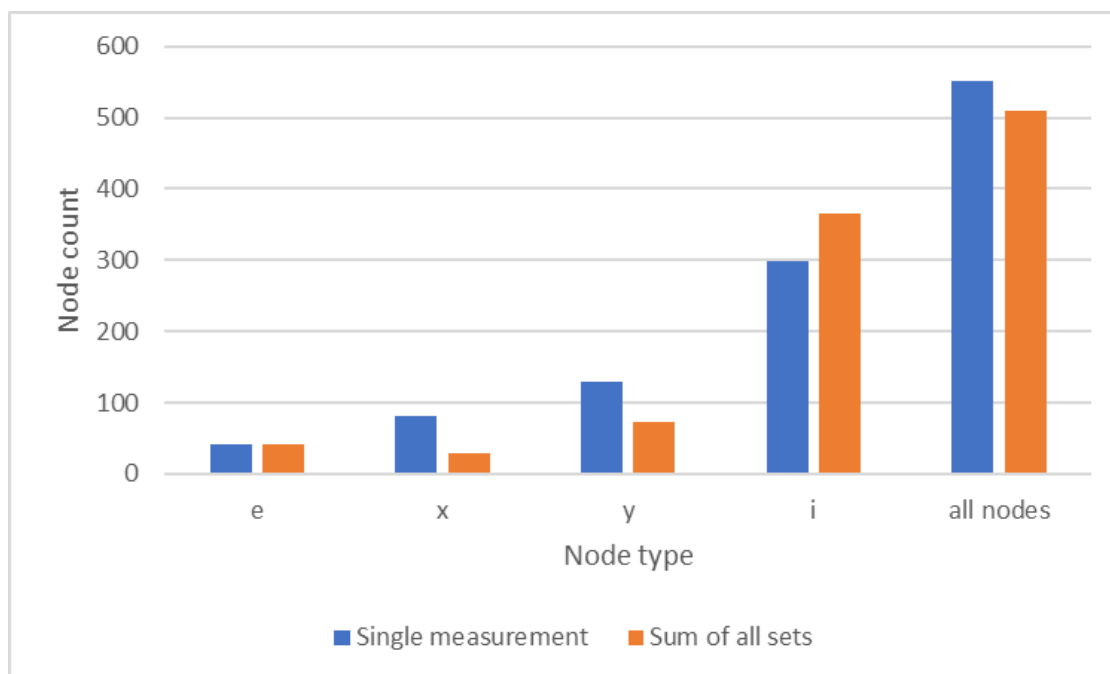
381 Topological analysis of all the fractures was undertaken in a measurement
 382 circle and all the nodes, including those formed between different fracture
 383 sets, were accounted for at the same time to define the true topological
 384 characteristics. Table 4 and Figure 4 demonstrate that not considering all
 385 the nodes in a single measurement will result in an under-accounting of the
 386 intersecting "x" and "y" nodes, an over-accounting of the number of "i"
 387 nodes and an under-estimate of the total number of nodes. This will affect
 388 the calculation of the topological characteristics.

389
 390 Table 4: Number of nodes measured when considering all fracture sets
 391 together in a single measurement compared to summing the number of
 392 nodes of individual fracture sets from Site 3. The number of "e" is the same,
 393 "x" and "y" nodes are more common in the former and "i" in the latter. This
 394 indicates a greater number of intersections are present when all fractures
 395 are considered together. The ratio of nodes changes, altering the
 396 topological characteristics.

| | Node type | e | x | y | i | all |
|--------------------|---------------|----|----|----|-----|-----|
| Single measurement | Unmineralised | 19 | 48 | 71 | 97 | 235 |
| | Mineralised | 23 | 33 | 58 | 202 | 316 |

| | | | | | | | |
|-------------|------------|---------------|----|----|-----|-----|-----|
| | | Total | 42 | 81 | 129 | 299 | 551 |
| Set 1 | > 25 cm | Unmineralised | 8 | 0 | 6 | 14 | 28 |
| | | Mineralised | 7 | 3 | 9 | 36 | 55 |
| | | Total | 15 | 3 | 15 | 50 | 83 |
| Set 2 | 10 - 25 cm | Unmineralised | 10 | 2 | 6 | 58 | 76 |
| | | Mineralised | 4 | 3 | 10 | 51 | 68 |
| | | Total | 14 | 5 | 16 | 109 | 144 |
| Set 3 | < 10 cm | Unmineralised | 1 | 17 | 17 | 110 | 145 |
| | | Mineralised | 12 | 4 | 25 | 97 | 138 |
| | | Total | 13 | 21 | 42 | 207 | 283 |
| Sum of sets | | Unmineralised | 19 | 19 | 29 | 182 | 249 |
| | | Mineralised | 23 | 10 | 44 | 184 | 261 |
| | | Total | 42 | 29 | 73 | 366 | 510 |

397



398

399 Figure 4: Number of different types of nodes present at Site 3, according
400 to measurement type. The ratios and total number of nodes is different if
401 all fractures are considered in a single measurement.

402 *3.2 Determination of fractal dimensions*

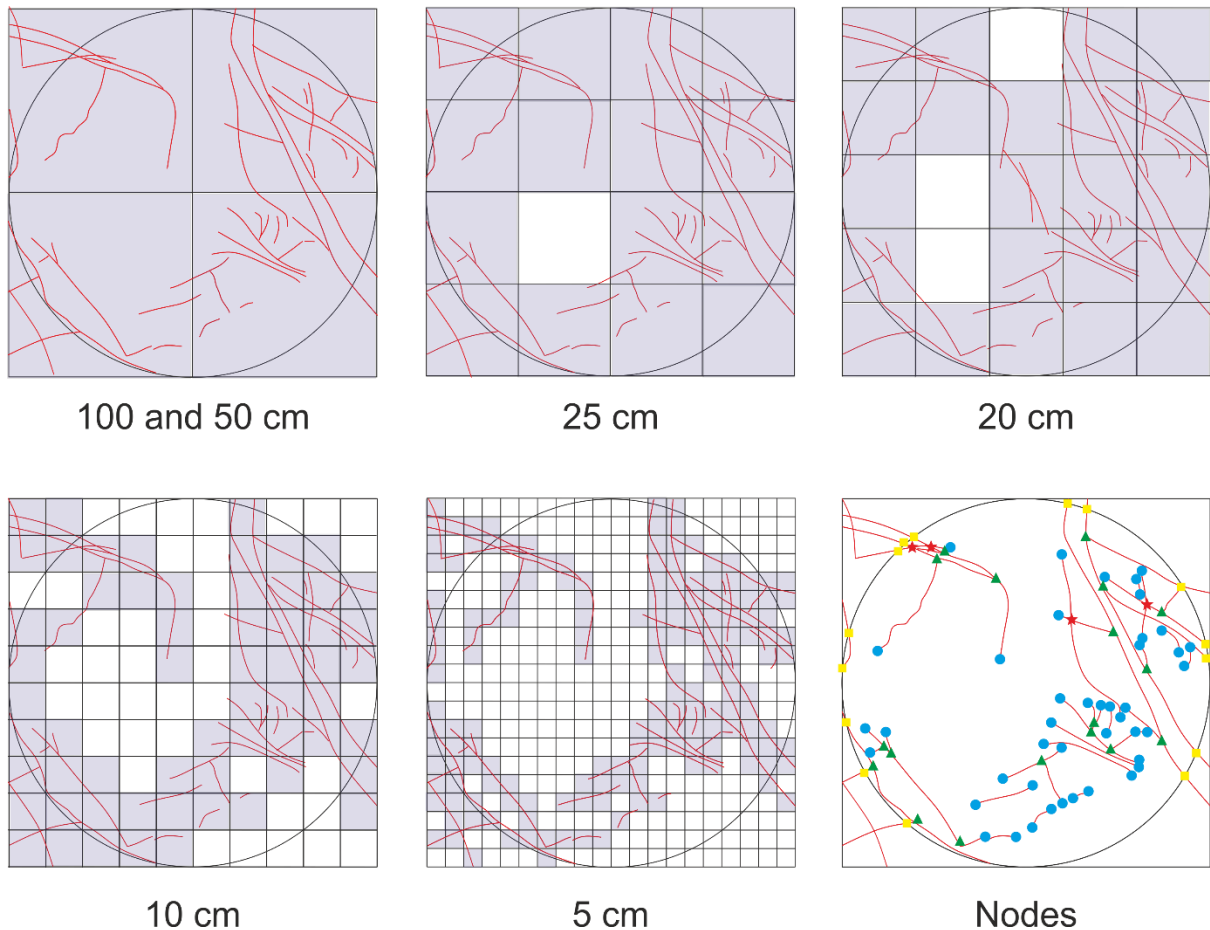
403 Complex scale-independent shapes can be quantified relative to the spatial
404 dimension (1D, 2D or 3D) in which they are observed. The intermediate
405 dimensions are referred to as fractal dimensions and have values between
406 the dimensions of the objects and the dimensions in which the objects are
407 observed. In this work, fractal dimensions are between one (the dimension
408 of a fracture line) and two (the dimensions of the measurement surface).

409 In this study, fractal dimensions are calculated using a scale-independent
410 box-counting method as defined by Mandelbrot (1967) and employed by
411 many authors to characterise fractures (e.g. Cahn, 1989; Kagan, 1991;
412 Odling, 1994; Berntson and Stoll, 1997; Libicki and Ben-Zion, 2005; Zhang,
413 2020). Other methods for the calculation of fractal dimensions, such as the
414 probability-density (Nykamp, 2020) or pair correlation functions (Satoh,
415 2003), which compare the number of points closer together than a specific
416 distance with the total number of points, may also be employed.
417 Importantly, the fractal dimension calculated using the box counting and
418 the pair correlation methods have the same average values (Mou and
419 Wang, 2016). The point analysis methods are typically utilised where there
420 is uncertainty in the validity of the much simpler and more widely
421 recognised box-counting methods.

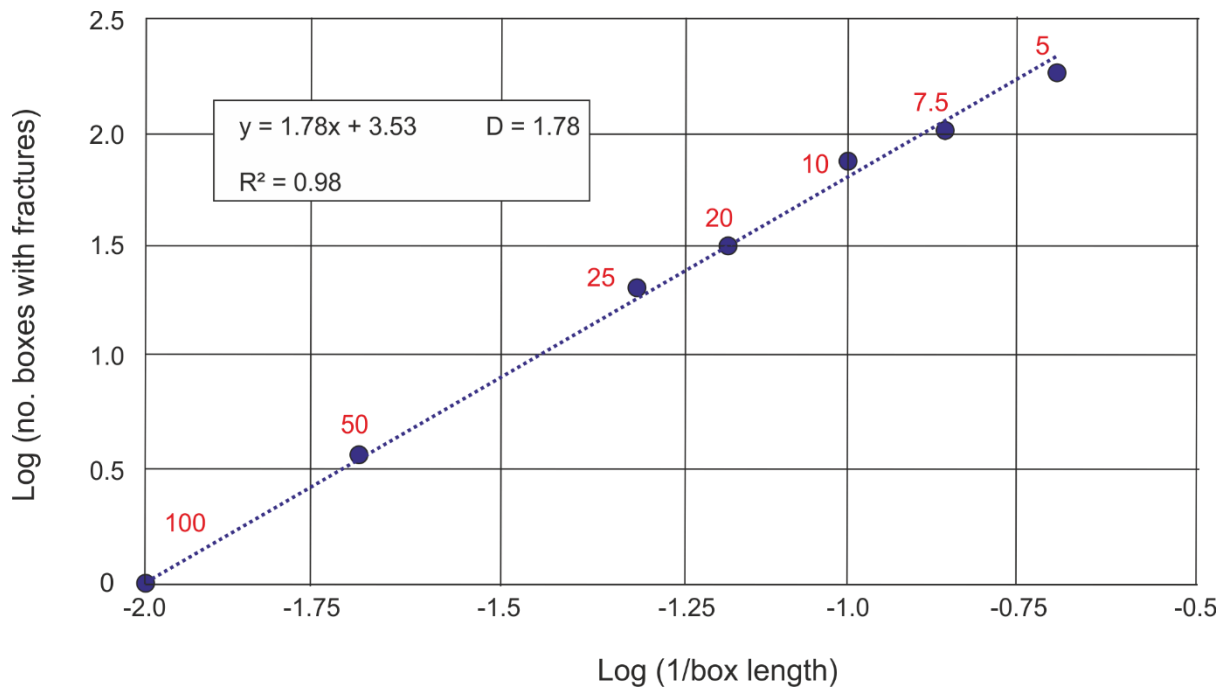
422 1 m-by-1 m measurement squares with grids of different box-sizes are
423 placed over the 1 m diameter topology measurement circles, and the
424 number of boxes containing fracture traces counted (Figure 5). Following
425 the methodology of Walsh and Watterson (1993), the measurement
426 squares do not extend beyond the edge of the fractured portion of the rock.
427 Although the box counting squares do not cover the same areas as the 1
428 m diameter topological measurement circles, the squares are centred on
429 the circles and the same size squares are analysed for the different box
430 sizes, thus providing comparable data.

431 The slope of the log-log plot of the inverse of the box length versus the
432 number of boxes containing fractures at each box size (Figure 6) is defined

433 as the box-counting fractal dimension (Foroutan-pour *et al.*, 1999). Trend
434 lines with correlation coefficients of at least 0.98 are generally considered
435 to be representative of the fractal dimension (Liang *et al.*, 2012; Zhihui *et*
436 *al.*, 2013). A slightly lower minimum correlation coefficient of 0.95 was
437 considered acceptable in this study, given the comparatively smaller scale
438 range of box sizes used (Figure 6).



439
440
441 Figure 5: Box counting grids (grid size indicated beneath each circle) are
442 placed over a measurement circle and only boxes that contain a fracture
443 trace are summed (shaded boxes) and used to determine the box-counting
444 fractal dimension. The associated topological node data are also shown (see
445 Figure 3 for description of node symbol colours and shapes). Nodes outside
446 of the circle are not considered in the topological analysis.
447



448

449 Figure 6: Log-log plot of data from Site 4. The gradient of the best-fit trend-
 450 line is the fractal dimension of these data. Red numbers indicate box side
 451 length in centimetres.

452 If the box sizes are too large or too small then the gradient of the trend-
 453 line may form a plateau at either end of the plot (Walsh and Watterson,
 454 1993). No significant changes in the gradient of the trend-lines were
 455 observed for all sites in this study. Thus, the box size distribution of
 456 between 5 cm and 1 m is considered appropriate for these lithologies in this
 457 context.

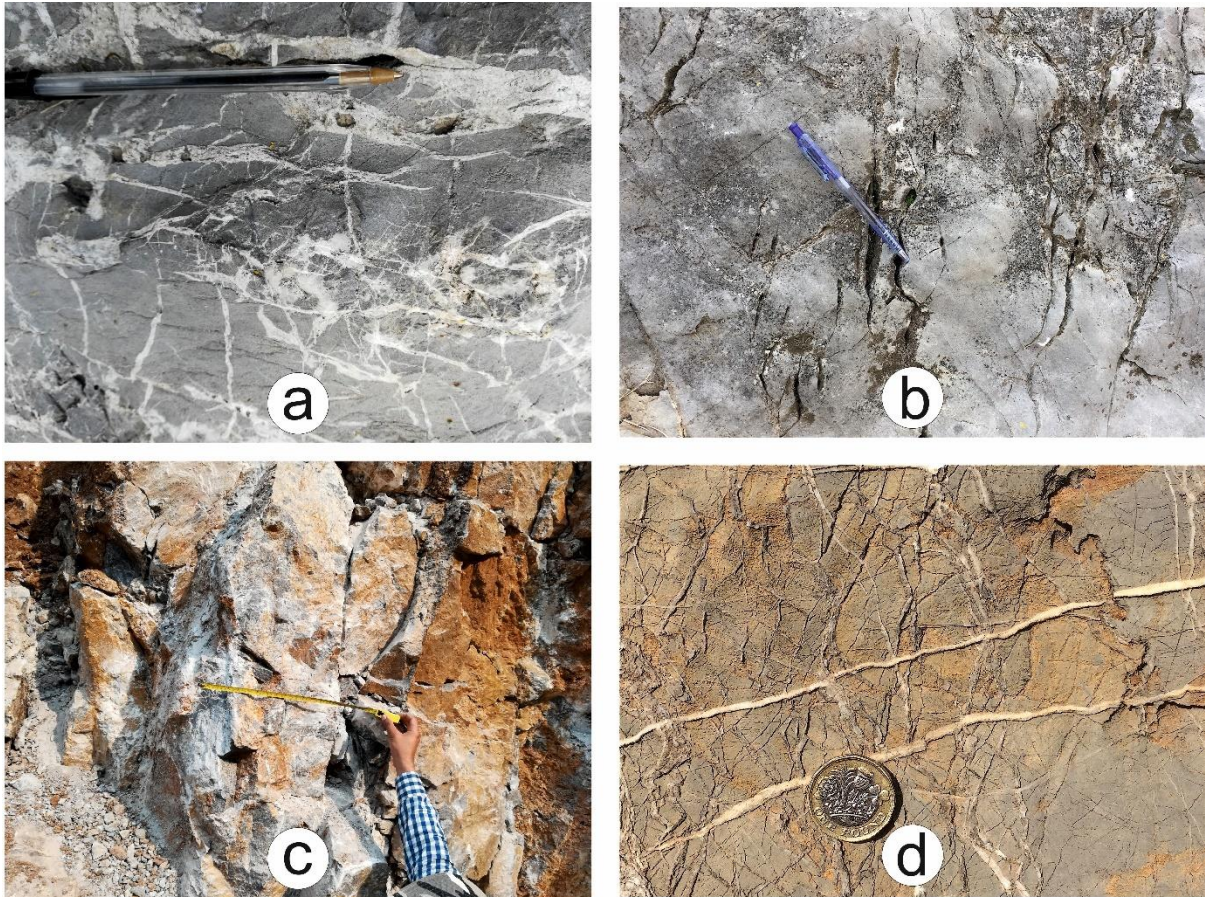
458

459 **4. Fracture characteristics of the study sites**

460 Four principal fracture types are observed in the limestone rocks examined
 461 in this study (Figure 7):

- 462 (a) Explosive, hydro-fracture-type calcite-filled veins without any
- 463 dominant orientation trends,
- 464 (b) unmineralised clusters of sub-parallel fractures,

- 465 (c) clay- or gouge-filled shear fractures typically oriented parallel to
466 bedding or with multiple cross-cutting relationships close to folds
467 and thrusts,
468 (d) sub-parallel, calcite-filled veins that increase in abundance with
469 proximity to thrusts of large displacement.
470



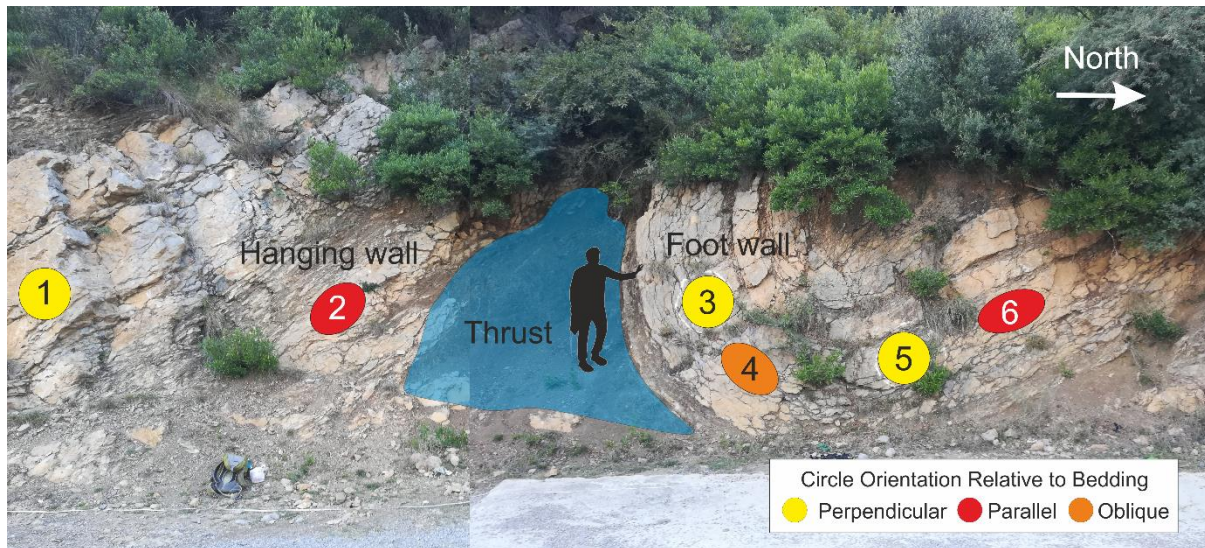
471
472 Figure 7: Principal fracture types of this study. (a) explosive hydro-
473 fractures, (b) unmineralised clusters of sub-parallel extension fractures, (c)
474 clay / gouge filled shear fractures, (d) sub-parallel calcite-filled veins. These
475 principal fracture types can occur individually or combine as pairs, or as
476 fracture systems of three or four different principal types.

477 These principal fracture types are present at all sites studied and occur
478 individually or combine as pairs, or as fracture systems of three or four
479 different principal types.

480

481 **4.1. Characteristics of total fracture sets**

482 Site 1 is located 500 m north of the Himalayan MBT (Figure 2). The site
483 consists of tightly folded limestone units of the Lockhart Formation (Figure
484 8). A highly deformed shaly siltstone unit, with centimetre-thick,
485 structurally induced laminations, forms a decollement surface over the
486 tightly folded 0.4 m thick limestone beds.



487

488 Figure 8: Site 1 - tightly folded limestone units (circles 3, 4, 5 and 6) and
489 siltstone with limestone (circles 1 and 2) overthrust northwards. The
490 measurement circles, with their associated box-counting squares, are in
491 different orientations relative to bedding (see also Table 3).

492 Although there is little difference in the total number of nodes measured in
493 each of six circles placed across the structure at Site 1 (Figure 8) the
494 proportions of different types of nodes vary between circles relative to their
495 orientation and distance from the thrust as displayed in Appendix 1 which
496 also details these characteristics for all the mapping sites. In the hanging
497 wall of the thrust at Site 1 (Circle 1), there are very few X nodes formed
498 from cross-cutting fracture traces, but equal numbers of Y and I nodes
499 formed from fracture terminations. Towards the thrust (Circle 2) E, X and
500 Y nodes increase in proportion relative to I nodes. In the footwall of the
501 thrust (Circles 3 to 6) the measurement circles have similar numbers of
502 nodes to each other and further from the thrust, the fractures display a

503 progressive increase in connectivity but decrease in fracture density. The
504 fractal dimension is 1.88 at this site.

505 Site 2 is only 400 m away from Site 1 (Figure 2), but the structural geology
506 is significantly different. Interbedded limestone and shaly siltstone of the
507 Lockhart Formation are folded into a tight, upright anticline with a
508 wavelength of approximately 20 m and an amplitude of approximately
509 60 m. The sedimentary succession consists of beds of argillaceous
510 limestone, each on average 20 cm thick, combining to form 60 cm thick
511 units bounded by centimetre-thick laminated mudstone units, younging
512 into alternating packstone and dark-grey wackestone beds, each
513 approximately 10 cm thick. The strongly laminated wackestone has a high
514 fracture intensity, but a low number of branches due to bedding-parallel
515 failure along the thin shaly units. The lack of cross-cutting fractures reduces
516 the connectivity of fracture network. Due to the interlayered nature of the
517 limestone and mudstone lithologies, the site displays a wide range in fractal
518 dimensions of between 1.72 and 1.92. Although some of the thinner
519 limestone units have fractal dimensions of greater than 1.8, most of the
520 rock mass deformation has deformed through shearing along bedding
521 planes, reducing the fractal dimension. This fracture pattern also results in
522 a lower fracture density as much of the applied stress is accommodated by
523 shearing, rather than by the development of additional fractures.

524 Site 3 is located in a succession of 1.5 m thick limestone beds of the
525 Lockhart Formation. The presence of a single, large, through-going fracture
526 results in a high degree of connectivity, and a high fractal dimension of
527 1.97 (virtually a 2D plane). In contrast to this, numerous fractures that are
528 less than 1 mm wide have high intensity but low connectivity. The abundant
529 small fractures also cause a low overall mean trace length for the site.

530 Site 4 is situated in a relatively undeformed pop-up anticline bounded
531 between sets of fore-thrusts and back-thrusts (Figure 2). The limestone
532 units of the Lockhart Formation at this site consist of packstone beds –
533 approximately 30 cm thick – dipping 14 degrees towards the south-south-

534 west. The topological characteristics and the fractal dimension of the
535 bedding-plane parallel fractures closely match those of the bedding-
536 perpendicular fractures.

537 The broad, easily accessible back-thrust thrust surface formed on an
538 approximately 1 m thick limestone bed at Site 5 has prominent calcite veins
539 developed both parallel to and perpendicularly to the thrust on the exposed
540 surface. The dominant thrust-parallel calcite-filled fractures and thicker
541 thrust-perpendicular fractures (that are also therefore parallel to the fault
542 propagation fold axis) are more widely spaced and the mean trace length
543 is approximately half that of the sites in the fore-thrust. Small, millimetre-
544 thick, calcite-filled fractures with short trace lengths of up to 5 cm are
545 common throughout in a variety of different orientations resulting in a large
546 number of nodes. The different topological and fractal details of these
547 elements are combined to define the general rock mass behaviour of the
548 back-thrust. The observed fractures have the highest number of branches
549 (264) and highest fracture intensity (20.7) and density (37.9) of all the
550 measurement sites. They are also characterised by a shorter mean trace
551 length (14) than Sites 1,2,3, and 10 in the fore-thrust. Due to the high
552 degree of fracturing, the site has a high fractal dimension of 1.93.

553 Site 6 is the most northerly mapping location and hence furthest from the
554 MBT. This site is dominated by limestone beds approximately 1 m thick,
555 with irregular centimetre-thick argillaceous siltstone partings that are
556 highly sheared. Several classic thrust structures are evident, including
557 relatively undeformed footwall strata immediately beneath the thrust
558 plane.

559 The thrust fault and the associated fault propagation fold zone at Site 6 are
560 both highly fractured. The footwall to the thrust comprises a foraminiferal
561 packstone that is typical of the upper stratigraphy of the Lockhart
562 Formation, which is only weakly deformed with discontinuous, variably
563 oriented, thin (1 mm or less) calcite-filled fractures. Thrust-parallel
564 fractures are present, none of which are mineralised, and there are very

565 few brittle tensile fractures associated with the thrust-related folding.
566 However, the rock mass within the fault propagation fold area is highly
567 fractured, iron oxide-rich bedding-parallel thrust surfaces and steeply
568 dipping fault propagation fold fracture planes. The limestone fragments
569 between these fractures all contain abundant scattered, millimetre-wide,
570 calcite-filled fractures.

571 The average fractal dimension of circular measurement windows from the
572 thrust footwall at Site 6 is 1.56. In the thrust hanging wall, the bedding-
573 and thrust-parallel fractures are better connected than the thin calcite-
574 cemented tensile fractures that display the highest number of tips, lines
575 and branches, and a high dimension of 1.92. When the measurements of
576 the folded hanging wall and thrust-plane itself are included, the dimension
577 increases from 1.56 to 1.80, which reflects the variability that occurs when
578 considering different parts of a geological structure. This variation accounts
579 for the overlap between the groupings based on the larger scale
580 descriptions of a geological structure, such as "fore-thrust", when individual
581 portions of a specific structure display different fractal properties. Despite
582 there being a high number of fracture intersections in the footwall (524 in
583 total), there are very few edge intersections (only 4%) and cross-cutting
584 fractures (7%). Moreover, 55% of the fractures do not terminate against
585 another fracture.

586 The Lockhart Formation is well exposed in the back-thrust at both Site 7
587 and Site 8 along strike from sites 5 and 6. The rocks of these sites consist
588 of highly fractured metre-thick, grey foraminiferal packstone that is less
589 intensely fractured than the other back-thrust sites resulting in lower fractal
590 dimensions (1.82 and 1.83).

591 The flat dipping centimetre thick mudstone beds of Site 9, exposed in a
592 river valley that runs perpendicular to the regional strike, have few
593 fractures and the lowest fractal dimension (1.76). This is due to a
594 combination of the stratigraphy (thinly bedded strata) and structural

595 setting (in a pop-up zone), with the limited applied stresses being released
596 by bedding parallel shearing.

597 At Site 10, the Lockhart Formation has been folded into an anticline with a
598 wavelength of approximately 10 m and an amplitude of 25 m. Flexural flow
599 has been facilitated by centimetre-thick mudstone-limestone layers,
600 reducing the number of fractures on the interbedded light-grey coloured
601 0.5 m thick limestone beds in this fore-thrust setting.

602

603 **5. Analysis of fractal and topological characteristics**

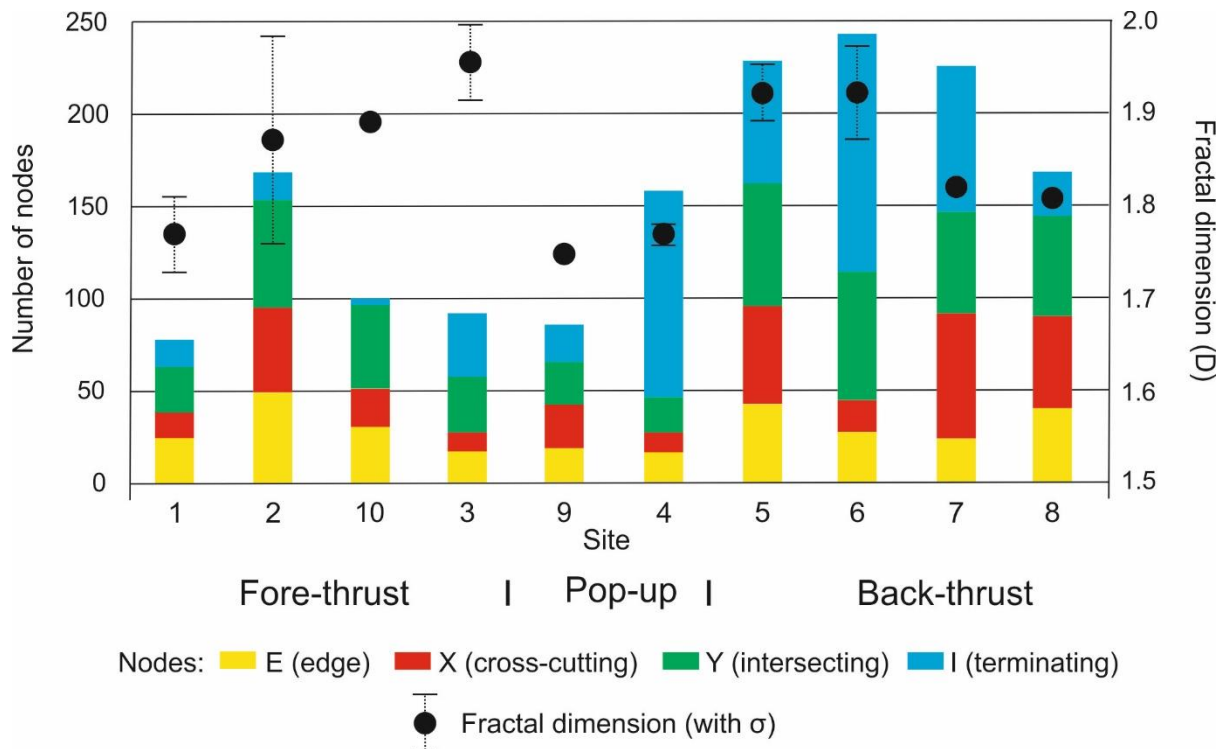
604 In order to understand how the fracture networks vary spatially across the
605 fold and thrust belt, the measured topological parameters and fractal
606 dimensions are cross-correlated. The data employed to undertake this
607 analysis are presented in Appendix 1.

608 Sites 1 to 6 are described in detail above as they provide an ideally oriented
609 distribution of successive structural domains from a fore-thrust, through a
610 pop-up to a back-thrust and the associated fracture patterns. Additional
611 data from four supplementary sites located along strike from the main
612 transect (Figure 1) have been included to confirm the characterisation of
613 the fracture pattern in different structural domains by using this
614 combination of the topological and fractal characteristics (see Figure 9).

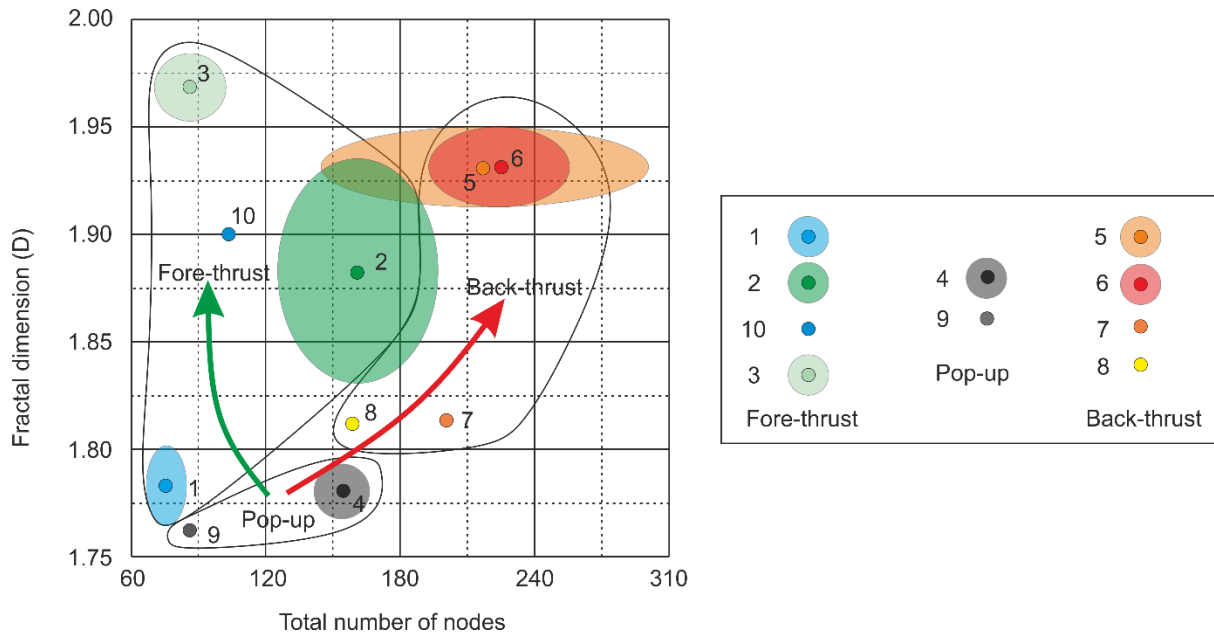
615 When the average fractal dimension and the average total number of nodes
616 of each type in the fracture network at each of the sites are examined,
617 characteristic values are apparent. The fore-thrust and pop-up structures
618 have lower total numbers of nodes than the back-thrusts, and the pop-up
619 has the lowest fractal dimension whilst the fractal dimension is higher in
620 both the fore-thrust and back-thrust (Figure 9).

621 By plotting, not just the average, but also the range of these values, cross-
622 plot correlations between fractal dimensions and total number of nodes

623 may be drawn (Figure 10) showing the trends in the changes in the
 624 characteristics of the fracture system.



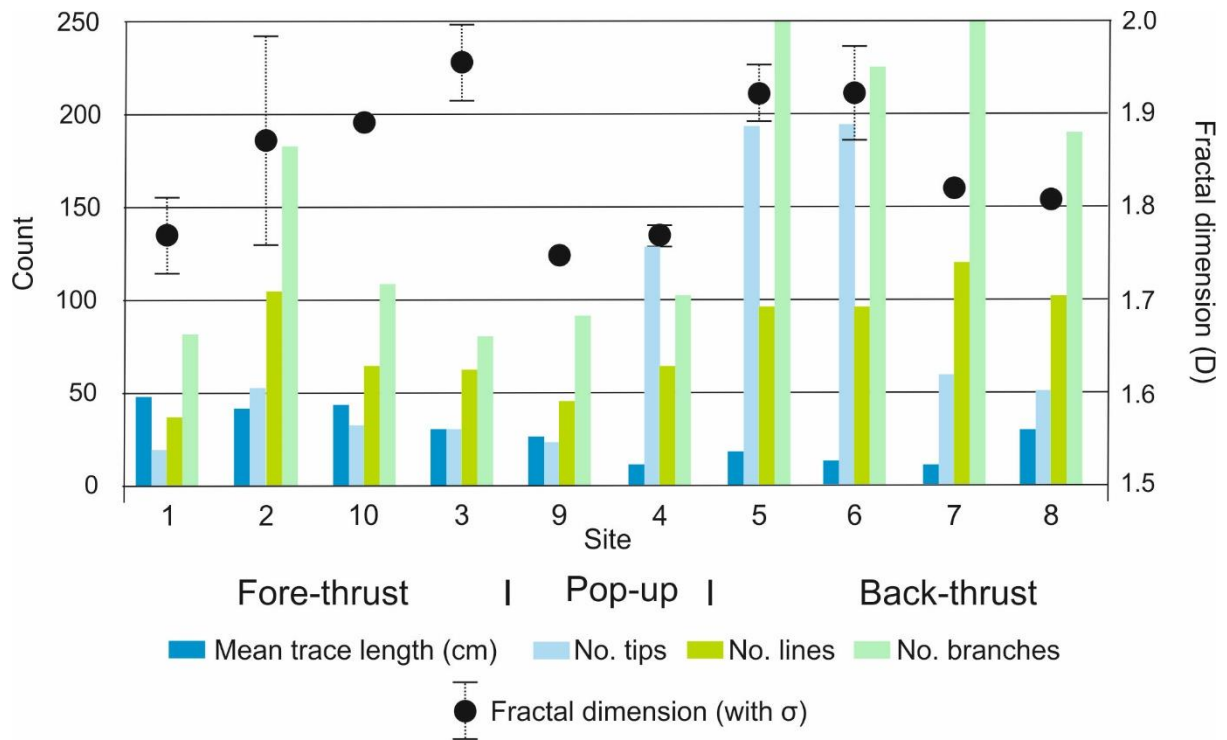
625
 626 Figure 9: Average number of nodes and fractal dimensions at each site,
 627 grouped according to structural domain. Note the greater number of nodes
 628 and proportion of I nodes at sites in the back-thrust structural domain. The
 629 fractal dimension is lowest in sites within the pop-up structural domain.



630

631 Figure 10: Average total number of nodes vs. average fractal dimension of
 632 the various sites in the different structural domains. The average values of
 633 datasets from each site are indicated by small bold circles and the standard
 634 deviations of the datasets are indicated by the more transparent ellipses of
 635 the same colour. Bold circles with no ellipses represent sites with a single
 636 measurement circle. Trends in the number of nodes and fractal dimension
 637 from the pop-up to the fore-thrust and back-thrusts are shown by the green
 638 and red arrows, respectively.

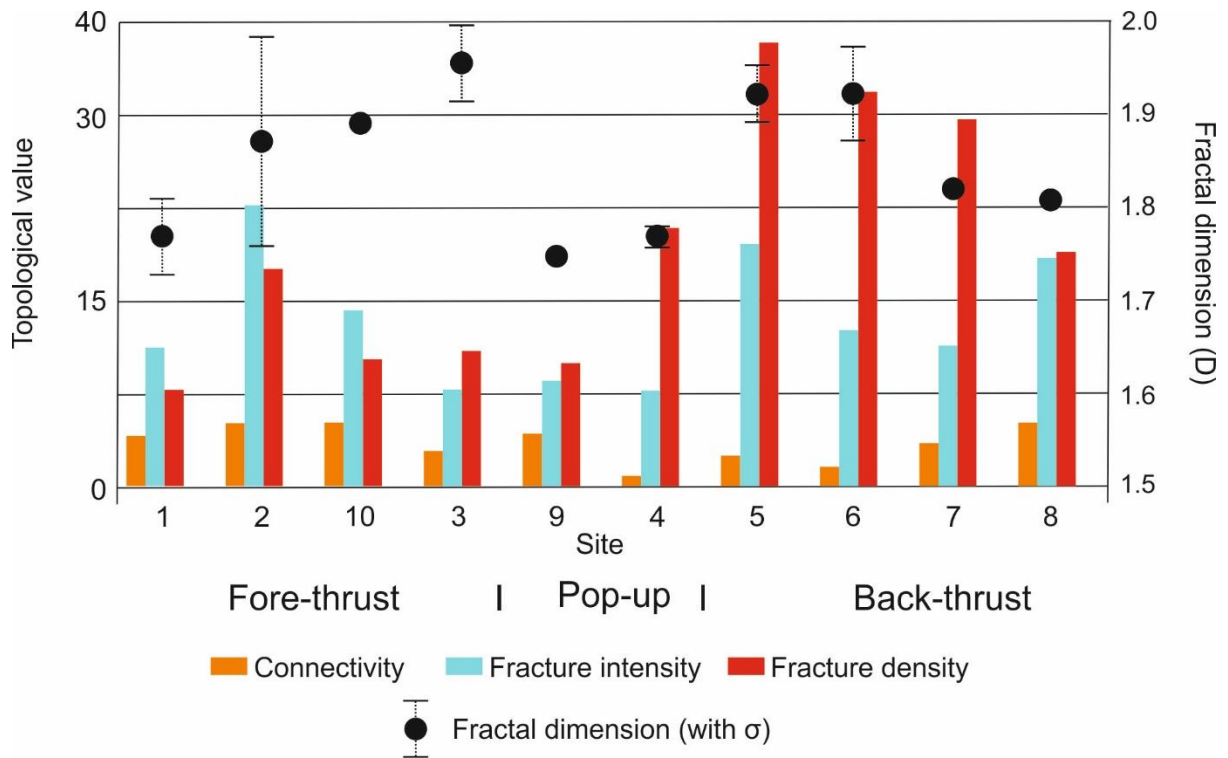
639 Figure 11 and Figure 12 show the variations in the fractal dimensions and
 640 topology of the different structural domains. The longer mean trace length
 641 in the fore-thrust and greater number of branches and higher fracture
 642 density in the back-thrust are evident on these graphs, as is the low fractal
 643 dimension of the pop-up structure.



644

645 Figure 11: Fracture characteristics (mean trace length, number of tips,
 646 lines, and branches) derived from the analysis of topological data and
 647 fractal dimensions for different sites.

648 The differences in the fractal dimension and fracture characteristics derived
 649 from the topology of the different structural domains are best shown by
 650 comparing them against each other graphically. The basic topological
 651 parameters of the number of tips, lines and branches are inputs into the
 652 fracture density, connectivity, intensity, and mean trace length which are
 653 plotted against the fractal dimensions to illustrate these relationships with
 654 the fractal dimension for the different structural settings in this study
 655 (Figure 13).

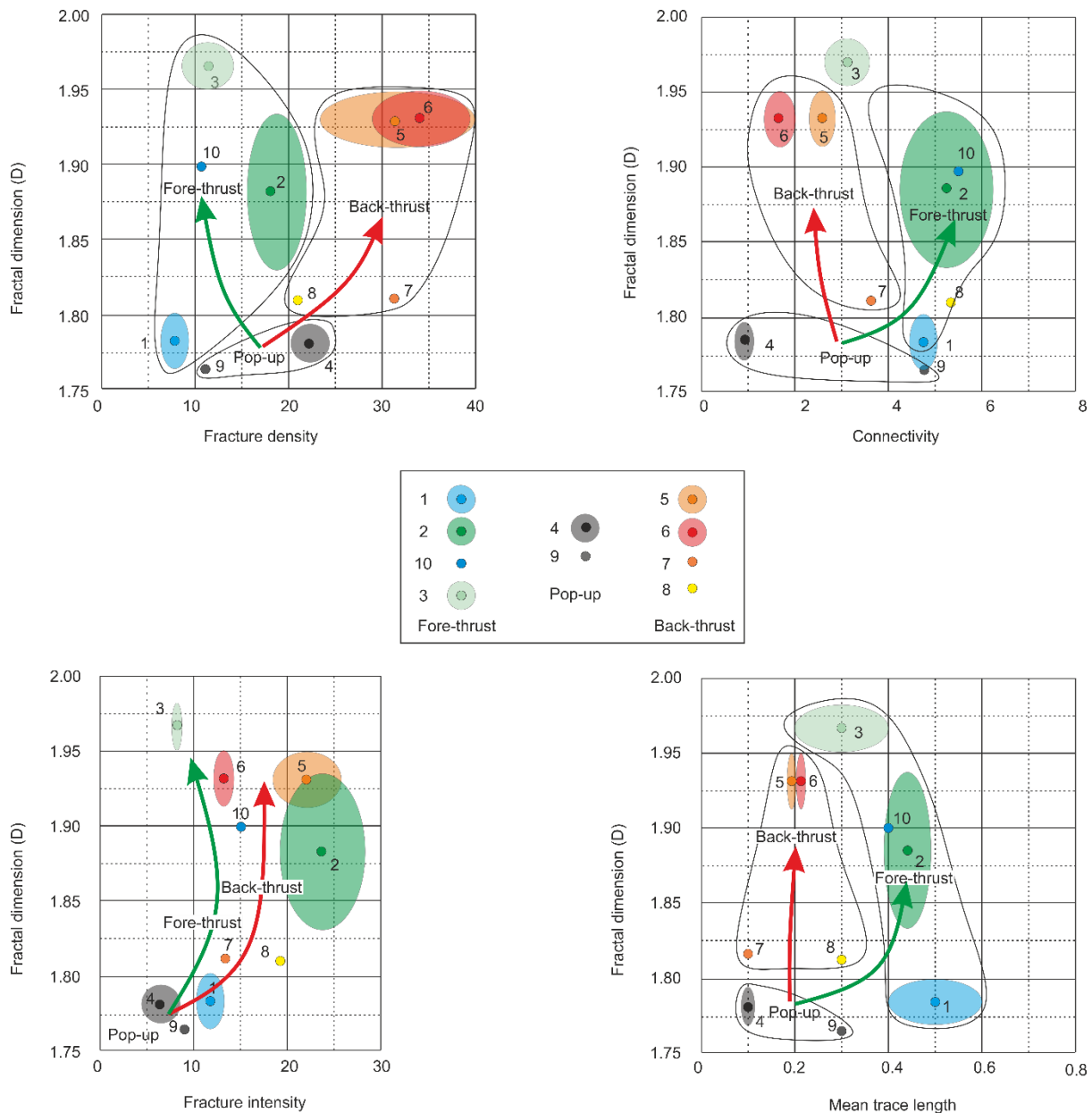


656

657 Figure 12: Fracture characteristics (connectivity, fracture intensity and
 658 fracture density) derived from the analysis of topological data and fractal
 659 dimensions for different sites.

660

661 When the average and range of topologically derived fracture
662 characteristics and fractal dimensions are considered in different structural
663 domains, distinct relationships are apparent (Figure 13 and Table 5). Fore-
664 thrusts are characterised by fewer, longer, well-connected fractures and
665 back-thrusts contain a higher number of fractures with more tips, lines, and
666 branches but these are not as well interconnected. The highest fractal
667 dimensions of the fore-thrust and back-thrust are immediately adjacent to
668 the pop-up zone (Figures 10 and 11). As the pop-up zone (sites 4 and 9)
669 between the fore-thrust and back-thrust has a lower fractal dimension and
670 also displays the lowest connectivity, fracture intensity and mean trace
671 length indicating that it is the least disturbed structural domain and can
672 thus be used as the starting point from which the characteristics of the fore-
673 and back-thrusts evolve and are superimposed (Figure 13).



674

675 Figure 13: Fractal dimension (D) compared to fracture characteristics
 676 derived from topological analysis of data from different structural domains.
 677 Average values of datasets from each site are indicated by bold circles and
 678 the standard deviations of the datasets are indicated by the more
 679 transparent ellipses of the same colour. Trends in the number of nodes and
 680 fractal dimension from the pop-up to the fore-thrust and back-thrusts are
 681 shown by the green and red arrows, respectively. There is good correlation
 682 between structural domain, fractal dimension and density, connectivity,
 683 and mean trace length. The correlation is poor when considering fracture
 684 intensity. It should be noted the reversed position of the fore-thrust and

685 back-thrust locations within the graphs of fracture density as opposed to
 686 connectivity and mean trace length is due to the quantifiably different
 687 changes of these topological parameters in the two locations.

688 Table 5: Summary of topological and fractal characteristics. Back-thrusts
 689 have the highest average node count for each type, resulting in higher
 690 fracture density and number of tips, lines and branches compared to fore-
 691 thrusts but both domains have a similar range of fractal dimensions.

| Structure | Characteristic |
|-------------|-----------------------------|
| Fore-thrust | Fewer I nodes |
| | Lower total number of nodes |
| | Longer mean trace length |
| | D lower further from pop-up |
| Pop-up | Few E nodes |
| | Low fracture intensity |
| | Low number of lines |
| | Low number of tips |
| | Low number of branches |
| | Lowest D |
| Back-thrust | More nodes of all types |
| | Higher fracture density |
| | More tips |
| | More lines |
| | More branches |
| | D lower further from pop-up |

692 The higher fracture density and lower connectivity and mean trace length
 693 apparent in the topological data of the back-thrusts (Sites 5, 6, 7 and 8) is
 694 due to the predominance of small, shorter fractures. The fore-thrusts (Sites
 695 1, 2, 3 and 10) display more, longer fractures with an associated increase
 696 in connectivity (Figure 13). Like the fractal dimension, the fracture intensity
 697 increases in both the fore-thrust and back-thrusts (Figure 13).

698 As the fractal dimension is a measure of the distribution of a feature, in this
699 case fractures, the similar range of values present in this work implies the
700 rock mass deformed in a similar manner. However, the different fracture
701 characteristics derived from the topological values indicate that the stress
702 is accommodated differently in the fore-thrust and back-thrust setting.
703 Intuitively, it is expected that fracture networks in the fore-thrust will have
704 more extended fractures (greater mean trace length), due to extended
705 periods of movement on the thrust sheets compared to back-thrust
706 settings, where fracture networks are more irregular with higher fracture
707 density, as a result of late-stage layer-parallel shortening.
708 The data presented here suggest that fore-thrusts are dominated by fewer
709 but longer fractures that are the product of flexural flow, whereas the back-
710 thrust appear to be dominated by tangential longitudinal failure. The low
711 fractal dimension of the pop-up structure and the accompanying highest
712 fractal dimension in the fore-thrusts and back-thrusts immediately adjacent
713 to it shows that the fractal dimension can be used as an indicator of the
714 proximity of change to a different structural domain.
715

716 **6. Discussion**

717 **6.1. Significance of the cumulative effect of fractures**

718 The methodology presented here is novel in that it quantifies the total rock
719 mass of the limestone, including the fracture system within it, in a single
720 set of measurements collected simultaneously on the fracture system. This
721 approach not only enables efficient collection of data, dramatically reducing
722 the time taken for data collection, but more importantly, it provides data
723 that characterise the cumulative effects of the fractures, which may have
724 resulted from multiple strength hardening or weakening processes, and
725 their impact on the subsequent rock failure response (Laubach *et al.*, 2009;
726 Corradetti *et al.*, 2015).

727 This is important, because from a geomechanical perspective, the
728 behaviour of the rock mass is the sum of all its constituent inhomogeneities,
729 including both lithological variation and all fracture sets. In each structural
730 domain there is a general brittle failure pattern due to the stress-path that
731 the rock mass has undergone (Everall and Sanislav, 2018). This will impact
732 on subsequent fracture patterns. For example, it is necessary to carefully
733 consider pre-existing fractures, possibly unrelated to folding, to build more
734 realistic conceptual fold–fracture models (Lacombe *et al.*, 2011). This
735 cumulative effect on the rock mass is especially relevant in successions
736 when deformation is progressive, with successive fracture sets reflecting
737 the rock response to cumulative strain. The formation of one fracture set
738 controls the initiation or arrest of subsequent sets in an evolving stress
739 regime by providing new stress concentrators and barriers for the
740 deforming system. Consequently, it is not surprising that the occurrence of
741 multiple sets of fractures is the rule rather than the exception in many fold
742 and thrust belts (Salvini and Storti, 2001; Florez-Niño *et al.*, 2005; Iñigo
743 *et al.*, 2012; Corradetti *et al.*, 2015; Burberry *et al.*, 2019). The combined
744 effect of all the fracture systems therefore needs to be considered in a
745 structural fracture analysis.

746

747 Fracture sets may form by sequential events and infilling, with earlier
748 discontinuities acting as mechanical boundaries (Bai and Pollard, 2000).
749 However, not all fractures of a particular set terminate on fractures of a set
750 that was developed immediately prior to it, making it difficult to recognise
751 fracture sets and hence define the mathematical laws that describe the
752 distribution of each fracture set (Guerrero *et al.*, 2010). We do not attempt
753 to discriminate between the different fractures, as characteristics such as
754 composition, orientation or termination relationships & styles may not be
755 unique to a set of fractures formed in response to one single deformation
756 event. Rather, by considering the numbers of all the different types nodes
757 and the fractal dimension of all the fractures together, one can be confident
758 that all the various discontinuity constituents of the rock mass are
759 included.

760 In the case of the data set from the Lockhart Formation limestone
761 associated with the MBT, it is apparent that the standard deviation of the
762 number of nodes of different fracture sets is significantly lower than the
763 standard deviation of a group of all of the nodes of a fracture network. This
764 provides quantitative evidence that only analysis of all fractures within the
765 deformed rock volume is representative of the true complexity of the
766 system and therefore mostly likely to be able to characterise specific
767 structural domains.

768

769 **6.2. Recognition of structural domains from fracture analysis**

770 In our examination of the Lockhart Formation in the hanging wall of the
771 MBT we demonstrate that the characteristics of the fracture systems in
772 different structural domains can be recognised when all the fracture data
773 are considered together. Fracture systems developed in both fore-thrusts
774 and back-thrust settings have higher fractal dimensions than those in a
775 pop-up structure. Hydro-fractures are present throughout all structural
776 domains and do not vary in abundance relative to the structural regime.
777 They probably represent slightly earlier phases of brittle deformation

778 caused by initial thrusting and uplift events that promoted reductions in the
779 confining stresses. Continued deformation allowed the other principal
780 fracture types to develop with the longer calcite fractures and shear
781 fractures forming close to thrusts. The unmineralised extension fractures
782 and sometimes the shear fractures are associated with folds. As different
783 fracture types formed contemporaneously, there is a complex interaction
784 and overlap of all of the fracture types in this active fold and thrust belt
785 which may not be easily resolved. Topologically, fracture networks in the
786 fore-thrust setting are characterised by fewer nodes and a longer mean
787 trace length, hence a lower density, but higher connectivity. By contrast,
788 the topological characteristics of the back-thrust setting are dominated by
789 more nodes producing a higher fracture density and lower mean trace
790 length and higher intensity. This is a result of the opposite vergence of the
791 back-thrusts causing further heterogeneity in the stress state. The pop-up
792 zone has an overall low fracture intensity.

793 By adopting an approach that considers both spatial and topological
794 properties of fractures a relationship between fracture network parameters
795 to structural domain is apparent. It is only by combining and comparing the
796 two data types that the characterisation of structural styles become
797 apparent. Moreover, the distinction of structural domains with fracture
798 systems that are a result of the cumulative effects of multiple fracturing
799 events is enhanced when all the constituent fracture sets that define the
800 true characteristics of the rock mass are considered together.

801

802 **7. Conclusions**

803 A new approach of combining independently derived topological and fractal
804 analyses of fracture networks has been developed to quantify the
805 characteristics of highly deformed limestone in the Himalayan fold and
806 thrust belt. This technique is employed to define the characteristics of
807 complex, heterogenous fracturing in various structural settings within the
808 hanging wall of the Himalayan Main Boundary Thrust north of Islamabad,

809 Pakistan which has applicability to a wide variety of fracture networks in
810 different tectonic settings. Moreover, this approach dramatically reduces
811 the time taken for data collection and provides large amounts of unbiased
812 data representative of fracture network characteristics.

813 By examining the topological characteristics and fractal dimension of all the
814 fractures together it is possible to distinguish and quantify the fracture
815 system of an area based on empirical evidence and use this to define
816 specific structural domains. In general, the fracture systems developed in
817 both fore-thrusts and back-thrust settings have higher fractal dimensions
818 than those in a pop-up structure. The fractal dimension of both thrust types
819 decreases away from the central pop-up zone. Topologically, the fracture
820 networks in the fore-thrust setting have on average, fewer nodes and a
821 longer mean trace length and hence a lower density, but higher
822 connectivity. By contrast, the topological characteristics of the back-thrusts
823 setting are dominated by more nodes producing a higher fracture density
824 and lower mean trace length and higher intensity. The pop-up zone has a
825 low fracture intensity.

826 This method represents a first attempt to relate fracture network
827 parameters to structural style by adopting a combined approach that looks
828 at both spatial and topological properties. It is only by combining and
829 comparing the two data types that the characterisation of structural styles
830 become apparent.

831 As a fracture system is not simply the sum of the sets of fractures, but also
832 the interactions between them, we have developed a methodology that
833 rapidly establishes the attributes of the overall rock mass. By combining
834 the topological and fractal characteristics of the fractures into a single
835 group, it avoids problems associated with the mis-identification and
836 grouping of fractures that are not spatially or temporally related and
837 thereby wholly representative of the rock mass in question. Through
838 quantifying the cumulative characteristics of all the fractures in a single set
839 of measurements, we can recognise different structural domains.

840 The utilisation of the methodology established in this study should be
841 applicable to comparable lithologies in thin-skinned fold and thrust belts
842 and a variety of different brittle structural settings across a range of scales
843 worldwide. This could be readily tested by using the same analytical
844 techniques presented in this work, in either outcrop or subsurface settings.
845 The technique could also be used to provide a quantitative description of
846 fracture networks which would be a use interest to rock engineers.

847

848 **8. Acknowledgements**

849 This research is funded by Orient Petroleum Incorporated (OPI) and by the
850 Acorn Fund at Keele University. OPI additionally provided logistical support
851 for fieldwork in Pakistan. We gratefully acknowledge the assistance of OPI
852 management and especially field geologists Muhammad Saleem and Israr
853 Azfal, along with driver Khalid Nazar, for their generous assistance in the
854 field. We thank John Walsh (Fault Analysis Group, University College
855 Dublin) who very kindly reviewed an earlier draft of the manuscript and
856 clarified our thinking. We also extend our thanks to John Cosgrove, David
857 Sanderson, editor Steve Laubach and the anonymous journal referees for
858 their insightful reviews which helped prepare earlier versions of the
859 manuscript for publication.

860

861 **9. References**

- 862 Acharyya, S.K., Saha, P., 2018. Himalayan Paleogene Foreland Basin, its
863 collision induced early volcanic history and failed rift initiation. *Journal*
864 *of Asian Earth Sciences* 162, 3-12.
- 865 Ali, F. 2014. Tectonic Evolution of the Margalla Hills and a Part of the South
866 Eastern Hazara Ranges, Pakistan. Unpublished Ph.D. dissertation,
867 University of Peshawar, Pakistan.
- 868 Awdal, A., Healy, D., Alsop, G.I., 2016. Fracture patterns and petrophysical
869 properties of carbonates undergoing regional folding: A case study from
870 Kurdistan, N Iraq. *Marine and Petroleum Geology* 71, 149-167.
871 <http://dx.doi.org/10.1016/j.marpetgeo.2015.12.017>.
- 872 Aydin, A., 2000. Fractures, faults, and hydrocarbon entrapment, migration,
873 and flow. *Marine and Petroleum Geology* 17 (7), 797-814.
874 [https://doi.org/10.1016/s0264-8172\(00\)00020-9](https://doi.org/10.1016/s0264-8172(00)00020-9).
- 875 Bai, T., Pollard, D.D., 2000. Fracture spacing in layered rocks: a new
876 explanation based on the stress transition. *Journal of Structural Geology*
877 22, 43-57.
- 878 Barton, N.R., Lien, R. and Lunde, J. 1974. Engineering classification of rock
879 masses for the design of tunnel support. *Rock Mech.* 6(4), 189-239.
- 880 Barros-Galvis, N., Villaseñor, P., Samaniego, F., 2015. Analytical modelling
881 and contradictions in limestone reservoirs: breccias, vugs, and
882 fractures. *Journal of Petroleum Engineering* Article ID 895786.
883 <https://doi.org/10.1155/2015/895786>.
- 884 Berntson, G., Stoll P., 1997. Correcting for finite spatial scales of self-
885 similarity when calculating the fractal dimensions of real-world
886 structures. *Proc. R. Soc. B Biol. Sci.* 264, 1531-1537.
887 <https://doi.org/10.1098/rspb.1997.0212>.
- 888 Bieniawski, Z.T. 1973. Engineering classification of jointed rock masses.
889 *Transactions South African Institute of Civil Engineers* 15, 335-344.

- 890 Burberry, C.M., Cannon, D.L., Cosgrove, J.W., Engelder, T., 2019. Fracture
891 patterns associated with the evolution of the Teton anticline, Sawtooth
892 Range, Montana, USA. In: Bond, C.E. and Lebit, H.D. (eds) Folding and
893 Fracturing of Rocks: 50 Years of Research since the Seminal Textbook
894 of J. G. Ramsay. Geological Society, London, Special Publications, 487.
895 First published online 31 January 2019. <https://doi.org/10.1144/SP487.12>.
896
- 897 Burg, J-P., Celerier, B., Chaudhry, N.M., Ghazanfar, M., Gnehm, F.,
898 Schnellmann, M., 2005. Fault analysis and paleostress evolution in large
899 strain regions: methodological and geological discussion of the south
900 eastern Himalayan fold-and-thrust belt in Pakistan. Journal of Asian
901 Earth Sciences 24, 445–467.
- 902 Cahn, R., 1989. Fractal dimension and fracture. Nature 338, 201 – 202.
903 <https://doi.org/10.1038/338201a0>.
- 904 Chatterjee, S., Bajpil, S., 2016. India's Northward Drift from Gondwana to
905 Asia During the Late Cretaceous-Eocene. Proc Indian Nat. Sci. Acad. 82,
906 479-487.
- 907 Corradetti, A., Girundo, M., Tavani, S., Iannace, A., Parente, M. Mazzol, S.,
908 Strauss, C., Torrieri, S., Pirmez, C., Giorgioni, M. 2015. Analysis of
909 Reservoir Scale Fracture Sets in Southern Italy's Carbonate Reservoir
910 Analogues, Monte Faito, Sorrento Peninsula (Southern Italy).
911 International Petroleum Technology Conference, Doha, Qatar, paper
912 Number: IPTC-18433-MS. <https://doi.org/10.2523/IPTC-18433-MS>.
- 913 Cosgrove, J. W., 2015. The association of folds and fractures and the link
914 between folding, fracturing and fluid flow during the evolution of a fold–
915 thrust belt: a brief review. In: Richards, F. L., Richardson, N. J.,
916 Rippington, S. J., Wilson, R.W., Bond, C. E. (eds) Industrial Structural
917 Geology: Principles, Techniques, and Integration. Geological Society,
918 London, Special Publications, 421.
919 <http://dx.doi.org/10.1144/SP421.11>.

- 920 Cox, S.F., 2005. Coupling between Deformation, Fluid Pressures, and Fluid
921 Flow in Ore-Producing Hydrothermal Systems at Depth in the Crust.
922 Economic Geology 100th Anniversary Volume 39-75.
- 923 Darcel, C., Bour, O., Davy, P., 2003. Stereological analysis of fractal
924 fracture networks. Journal Geophysical Research 108 (B9) 2451,
925 <http://doi:10.1029/2002JB002091>.
- 926 Dasti, N., Akram, S., Ahmad, I., Usman, M., 2018. Rock fractures
927 characterisation in the Khairi Murat Range, Sub Himalayan Fold and
928 Thrust Belt, North Pakistan. The Nucleus 55 (3) 115 – 127.
- 929 Dziggel, A., Otto, A., Kisters, A.F.M., Meyer, F.M., 2007. Tectono-
930 metamorphic controls on gold mineralisation in the Barberton
931 Greenstone Belt, South Africa: an example from the New Consort Gold
932 Mine. In Van Kranendonk, M.J., Smithies, R.H., Bennet, V.C., (eds)
933 Developments in Precambrian Geology (15). Elsevier B.V.
934 [https://doi:10.1016/S0166-2635\(07\)15058-1](https://doi:10.1016/S0166-2635(07)15058-1).
- 935 Engelder, T., 1985. Loading paths to joint propagation during a tectonic
936 cycle: an example from the Appalachian Plateau, USA. Journal of
937 Structural Geology 7(3-4), 459-476.
- 938 English, J.M., Laubach, S.E., 2017. Opening-mode fracture systems -
939 Insights from recent fluid inclusion microthermometry studies of crack-
940 seal fracture cements. In Turner, J.P., Healy, D., Hillis, R.R., and Welch,
941 M., eds., Geomechanics and Geology: Geological Society, London,
942 Special Publications 458, 257-272. <https://doi:10.1144/SP458.1>.
- 943 Overall, T.J., Sanislav, I.O., 2018. The influence of pre-existing deformation
944 and alteration textures on rock strength, failure modes and shear
945 strength parameters. Geosciences 8 1-23.
946 <https://doi.org/10.3390/geosciences804024>.
- 947 Ferrill, D.A., Morris, A.P., Wigginton, S.S., Smart, K.J., McGinnis, R.N.,
948 Lehrmann, D., 2016. Deciphering thrust fault nucleation and
949 propagation and the importance of footwall synclines. Journal of

950 Structural Geology 85, 1-16.
951 <http://dx.doi.org/10.1016/j.jsg.2016.01.009>.

952 Florez-Niño, J-M, Aydin, A., Mavko, G., Antonellini, M., Ayaviri, A. 2005.
953 Fault and fracture systems in a fold and thrust belt: An example from
954 Bolivia. AAPG Bulletin 89 (4) 471–493.
955 <https://doi.org/10.1306/11120404032>.

956 Foroutan-pour, K., Dutilleul, P. Smith, D.J., 1999. Advances in the
957 implementation of the box-counting method of fractal dimension
958 estimation. Applied Mathematics and Computation 105 (2–3) 195-210.

959 Ghani, H., Zeilinger, G., Sobel, E.R., Heidarzadeh, G., 2018. Structural
960 variation within the Himalayan fold and thrust belt: A case study from
961 the Kohat-Potwar Fold Thrust Belt of Pakistan. Journal of Structural
962 Geology 116, 34-46.

963 Grodner, M. 1999. Fracturing around a deep level gold mine preconditioned
964 stope. Geotechnical and Geological Engineering 17, 291-304.

965 Guerriero V, Iannace, A, Mazzoli, S., Parente, M., Vitale, S., Giorgioni, M.,
966 2010. Quantifying uncertainties in multi-scale studies of fractured
967 reservoir analogues: Implemented statistical analysis of scan line data
968 from carbonate rocks. Journal of Structural Geology 32, 1271-1278.

969 Halley, J. M., Hartley S., Kallimanis A. S., Kunin, W. E., Lennon, J. J.,
970 Sgardelis, S. P., 2004. Uses and abuses of fractal methodology in
971 ecology. Ecology Letters 7, 254–271. [https://doi:10.1111/j.1461-](https://doi:10.1111/j.1461-0248.2004.00568.x)
972 [0248.2004.00568.x](https://doi:10.1111/j.1461-0248.2004.00568.x).

973 Hancock, P. L., 1985. Brittle microtectonics: principles and practice. Journal
974 of Structural Geology, 7(3-4), 437-457.

975 Hanif, M. Ali, F. Afridi, B.Z., 2014. Depositional environment of the Patala
976 Formation in biostratigraphic and sequence stratigraphic context from
977 Kali Dilli Section, Kala Chitta Range, Pakistan. Journal of Himalayan
978 Earth Sciences 46(1) 55-65.

- 979 Hoek, E. and Brown, E.T., 1980. Underground Excavations in Rock.
980 Institution of Mining and Metallurgy, London, 527 pp.
- 981 Hooker, J.N., Laubach, S.E., Marrett, R., 2013. Fracture-aperture sized
982 frequency, spatial distribution, and growth processes in strata-bounded
983 and non-strata-bounded fractures, Cambrian Mesón Group, NW
984 Argentina. *Journal of Structural Geology* 54, 54-71.
- 985 Iñigo, J.F., Laubach, S.E., Hooker, J.N., 2012. Fracture abundance and
986 patterns in the Subandean fold and thrust belt, Devonian
987 Huamampampa Formation petroleum reservoirs and outcrops,
988 Argentina, and Bolivia. *Marine and Petroleum Geology* 35(1), 201-218.
- 989 Iqbal, M., Bannert, D., 1998. Structural Observations of the Maragala Hills,
990 Pakistan and the Nature of the Main Boundary Thrust: *Pakistan Journal*
991 *Hydrocarbon Research* 10, 41-53.
- 992 Kagan, Y. Y., 1991. Fractal dimension of brittle fracture. *Journal of Non-*
993 *linear Science* 1, 1-16.
- 994 Korvin, G., 1989. Fractured but not fractal: fragmentation of the Gulf of
995 Suez basement. *Pure and Applied Geophysics* 131, 289-305.
- 996 Ladeira, F. L. and Price, N. J., 1981. Relationship between fracture spacing
997 and bed thickness. *Journal of Structural Geology* 13, 179-83.
- 998 Laubach, S.E., Olson, J.E., Gross, M.R., 2009. Mechanical and fracture
999 stratigraphy. *AAPG Bulletin* 93(11), 1413-1426.
- 1000 <http://doi:10.1306/07270909094>.
- 1001 Laubach, S.E., Olson, J.E., Eichhubl, P., Fomel, S., Marrett, A., 2010.
1002 Natural Fractures from the Perspective of Diagenesis. Focus Article
1003 CSEG Recorder September 2010, 26-31.
- 1004 Laubach, S.E., Lamarche, J., Gauthier, B.D.M., Dunne, W.M., Sanderson,
1005 D.J., 2018. Spatial arrangement of faults and opening-mode fractures.
1006 *Journal of Structural Geology* 108, 2-15.
- 1007 <http://dx.doi.org/10.1016/j.jsg.2017.08.008>.

1008 Laubach, S. E., Lander, R. H., Criscenti, L. J., Anovitz, L. M., Urai, J. L.,
1009 Pollyea, R. M., Hooker, J. N., Narr, W., Evans, M. A., Kerisit, S. N.,
1010 Olson, J. E., Dewers, T., Fisher, D., Bodnar, R., Evans, B., Dove, P.,
1011 Bonnell, L.M., Marder, M.P., Pryak-Nolte, L., 2019., The Role of
1012 Chemistry in Fracture Pattern Development and Opportunities to
1013 Advance Interpretations of Geological Materials. *Reviews of Geophysics*
1014 57(3), 1065-1111. <https://doi.org/10.1029/2019RG000671>

1015 Laubscher, D.H., 1977. Geomechanics classification of jointed rock masses
1016 -mining applications. *Transactions of the Institute of Mining and*
1017 *Metallurgy* 86, A1-8.

1018 Liang, Z., Feng, Z., Guangxianga, X., 2012. Comparison of Fractal
1019 Dimension Calculation Methods for Channel Bed Profiles. *Procedia*
1020 *Engineering* 28, 252 – 257. <https://doi:10.1016/j.proeng.2012.01.715>.

1021 Libicki, E. Ben-Zion, Y., 2005. Stochastic Branching Models of Fault
1022 Surfaces and Estimated Fractal Dimensions. *Pure and Applied*
1023 *Geophysics* 162 1077–1111.

1024 Long, J.C., Witherspoon, P.A., 1985. The relationship of the degree of
1025 interconnection the permeability in fracture networks. *Journal of*
1026 *Geophysical Research: Solid Earth* 90(B4), 3087–3098.

1027 Long, J.C.S., Aydin, A., Brown, S.R., Einstein, H.H., Hestir, K., Hsieh, P.A.,
1028 Myer, L.R., Kenneth G. Nolte, D.L., Olsson, O.L., Paillet, F.L., Smith,
1029 J.L., Thomsen, L., 1996. *Rock Fractures and Fluid Flow: Contemporary*
1030 *Understanding and Applications*. The National Academies Press,
1031 Washington, DC. <https://doi.org/10.17226/2309>.

1032 Mandelbrot B., 1967. How long is coast of Britain - statistical self-similarity
1033 and fractional dimension. *Science* 156, 636–638.

1034 Mauldon, M., Dunne, W.M., Rohrbaugh, M.B. Jr., 2001. Circular scanlines
1035 and circular windows: new tools for characterising the geometry of
1036 fracture traces. *Journal of Structural Geology* 23, 247-258.

- 1037 Mou, D., Wang, Z.W., 2016. Comparison of box counting and correlation
1038 dimension methods in well logging data analysis associate with the
1039 texture of volcanic rocks. Non-linear Processes Geophysics.
1040 Discussions. <https://doi:10.5194/npg-2014-85>.
- 1041 Nykamp, D.Q., 2020. The idea of a probability distribution. Math Insight.
1042 http://mathinsight.org/probability_distribution_idea.
- 1043 Odling, N.E., 1994. Natural Fracture Profiles, Fractal Dimension and Joint
1044 Roughness Coefficient. Rock Mech. Rock Eng. 27, 135-153.
1045 [https://doi: 10.1007/bf01020307](https://doi:10.1007/bf01020307).
- 1046 Odling, N. E., Gillespie, P., Bourgine, B., Castaing, C., Chiles, J. P.,
1047 Christensen, N. P., Fillion, E., Genter, A., Olsen, C., Thrane, L., Trice,
1048 R. Aarseth, E., Walsh, J. J., Watterson, J., 1999. Variations in fracture
1049 system geometry and their implications for fluid flow in fractures
1050 hydrocarbon reservoirs. Petroleum Geoscience 5, 373-384.
1051 <https://doi.org/10.1144/petgeo.5.4.373>.
- 1052 Ortega, O.J., Gale, J.F.W. Marrett, R., 2010. Quantifying diagenetic and
1053 stratigraphic controls on fracture intensity in platform carbonates: An
1054 example from the Sierra Madre Oriental, northeast Mexico. Journal of
1055 Structural Geology 32, 1943-1959.
- 1056 Peacock, D.C.P., Sanderson, D.J., 2018. Structural analyses and fracture
1057 network characterisation: seven pillars of wisdom. Earth Science
1058 Reviews, 184 13-28.
- 1059 Peacock, D.C.P., Sanderson, D.J., Rotevatn, A., 2018. Relationships
1060 between fractures. Journal of Structural Geology 106, 41-53.
- 1061 Pivnik, D. A., Wells, N.A., 1996. The transition from Tethys to Himalayas
1062 as recorded in NW Pakistan: Geological Society of America Bulletin 108,
1063 1295-1313.
- 1064 Pollard, D. D., Fletcher, R. C., 2005. Fundamentals of Structural Geology.
1065 Cambridge University Press, Cambridge, 500 pp.

- 1066 Procter, A., Sanderson, D.J., 2018. Spatial and layer-controlled variability
1067 in fracture networks. *Journal of Structural Geology* 108, 52-65.
- 1068 Ramsay, J.G., 1967., *The Folding and Fracturing of Rocks*. McGraw-Hill,
1069 New York.
- 1070 Redondo, J.M., Gonzalez-Nieto, P.L., Cano, J.L., Garzon, G.A., 2015. Mixing
1071 Efficiency across Rayleigh-Taylor and Richtmeyer-Meshkov Fronts.
1072 *Open Journal of Fluid Dynamics* 5, 145-150. [https://doi](https://doi.org/10.4236/ojfd.2015.52017)
1073 [10.4236/ojfd.2015.52017](https://doi.org/10.4236/ojfd.2015.52017).
- 1074 Renshaw, C.E., Pollard, D.D., 1994. Numerical simulation of fracture set
1075 formation: a fracture mechanics model consistent with experimental
1076 observations. *Journal of Geophysical Research* 99(18), 9359-9372.
- 1077 Robert J. L., Kazmi, A.H. and Jan. M.Q., 1997. *Geology and Tectonics of*
1078 *Pakistan*. Graphic Publisher, Karachi, 554 pp.
- 1079 Rouleau, A., Gale, J.E., 1985. Statistical characterization of the fracture
1080 system in the Stripa granite, Sweden. *International Journal of Rock*
1081 *Mechanics and Mining Sciences & Geomechanics Abstracts* 22(6), 353-
1082 367. [https://doi.org/10.1016/0148-9062\(85\)90001-4](https://doi.org/10.1016/0148-9062(85)90001-4)
- 1083 Salvini, F., Storti, F., 2001. The distribution of deformation in parallel fault-
1084 related folds with migrating axial surfaces: comparison between fault-
1085 propagation and fault-bend folding. *Journal of Structural Geology* 23
1086 (1). 25-32. [https://doi:10.1016/s0191-8141\(00\)00081-x](https://doi:10.1016/s0191-8141(00)00081-x).
- 1087 Sanderson D.J., Nixon C.W., 2015. The use of topology in fracture network
1088 characterisation. *Journal of Structural Geology* 72, 55-66.
1089 <http://dx.doi.org/10.1016/j.jsg.2015.01.005>.
- 1090 Sanderson, D.J., Peacock, D.C.P., Nixon, C.W., Rotevatn, A., 2019. Graph
1091 theory and the analysis of fracture networks. *Journal of Structural*
1092 *Geology* 125 155-165. <https://doi.org/10.1016/j.jsg.2018.04.011>.

- 1093 Satoh, A., 2003. Introduction to Molecular-micro stimulation of Colloid
1094 Dispersions, in Satoh, A. Studies in Interference Science, Volume 17.
1095 Elsevier Science, eBook ISBN 9780444514240.
- 1096 Silberschmidt, V.V., 1994. Fractal Characteristics of Joint Development in
1097 Stochastic Rocks pp 65 – 74. In Kruhl, J. H. (ed.), Fractals and Dynamic
1098 Systems in Geoscience. Springer-Verlag Berlin Heidelberg.
1099 <http://dx.doi.org/10.1007/978-3-662-07304-9>.
- 1100 Tariq, W., Rehman, G., Ahmad, S., Khan, M.I., Khan, S.F., 2017. Fracture
1101 porosity of the Lockhart Formation in the Nizampur Basin, KP, Pakistan.
1102 SPE PAPG Annual Technical Conference, 2017, Islamabad, pp 361 –
1103 374.
- 1104 Walsh, J.J., Watterson, J., 1993. Fractal analysis of fracture patterns using
1105 the standard box-counting technique: valid and invalid methodologies.
1106 Journal of Structural Geology 15(12), 1509–1512.
- 1107 Wandrey, C.J., Law, B.E., Shah, H.A., 2004. The Sembar Goru / Ghazij
1108 Composite Total Petroleum System, Indus and Sulaiman–Kirthar
1109 Geologic Ranges, Pakistan, and India. United States Geological Survey
1110 Bulletin 1: 1–20.
- 1111 Watkins, H., Bond, C.E., Healy, D., Butler, R.W.H., 2015. Appraisal of
1112 fracture sampling methods and a new workflow to characterise
1113 heterogeneous fracture networks at outcrop. Journal of Structural
1114 Geology 72, 67-82.
- 1115 Welch, M.J., Souque, C., Davis, R.K., Knipe, R.J., 2015. In Agar, S.M.,
1116 Geiger, S. (eds) Fundamental Controls on Fluid Flow in Carbonates:
1117 Current Workflows to Emerging Technologies.
1118 <https://doi.org/10.1144/SP406.5>.
- 1119 Wennberg, O. P., Svånå, T., Azizzadeh M., Aqrabi, A. M. M., Brockbank, P.,
1120 Lyslo K. B., Ogilvie S., 2006. Fracture intensity vs. mechanical
1121 stratigraphy in platform top carbonates: the Aquitanian of the Asmari

- 1122 Formation, Khaviz Anticline, Zagros, SW Iran. *Petroleum Geoscience*
1123 12(3), 235-246.
- 1124 Williams, V.S., Pasha, M.K. Sheikh, I.M., 1997. Geologic Map of the
1125 Islamabad-Rawalpindi Area, Punjab, Northern Pakistan. U.S.
1126 Department of the Interior. U.S. Geological Survey. Open-File Report
1127 99-47.
- 1128 Wu, H., Pollard, D.D. 1995. An experimental study of the relationship
1129 between joint spacing and layer thickness. *Journal of Structural Geology*
1130 17, 887– 905.
- 1131 Yeats, R. S., Hussain, A., 1987. Timing of structural events in the
1132 Himalayan foothills of north-western Pakistan. *Geological Society of*
1133 *America Bulletin* 99, 161–176.
- 1134 Zhang, Z., Xie, H., Zhang, R., Gao, M., Ai, T., Zha, E., 2020. Size and
1135 spatial fractal distributions of coal fracture networks under different
1136 mining-induced stress conditions. *International Journal of Rock*
1137 *Mechanics and Mining Sciences* 132, 104364.
1138 <https://doi.org/10.1016/j.ijrmms.2020.104364>.
- 1139 Zhihui, N. Lichun, W. Ming-hui, W., Jing, Y., Qiang, Z., 2013. The Fractal
1140 Dimension of River Length Based on the Observed Data. *Mathematical*
1141 *and Numerical Modelling of Flow and Transport* 2013, Article ID 327297.
1142 <https://doi.org/10.1155/2013/327297>